Changes in stream power and morphological adjustments at the event-scale and high spatial resolution along an ephemeral gravel-bed channel

Carmelo Conesa-García[1],* Carlos Puig-Mengual[2] , Adrián Riquelme[3] , Roberto Tomás[3], Francisco Martínez-Capel[2] , Rafael García-Lorenzo[1] , José L. Pastor[3], Pedro Pérez-Cutillas[1], Alberto Martínez-Salvador[1] and Miguel Cano-Gonzalez[3]

[1] Department of Physical Geography, University of Murcia, 30001 Murcia, Spain; rafaelgl@um.es (R.G.-L.); pedrope@um.es (P.P.-C.) aa.martinezsalvador@um.es (A.M.-S.)
[2]Institutd'Investigació per a la Gestió Integrada de ZonesCostaneres (IGIC), UniversitatPolitècnica de València (UPV), 46730 Gandia, Spain; carpuime@doctor.upv.es (C.P.-M.); fmcapel@dihma.upv.es (F.M.-C.)
[3] Department of Civil Engineering, University of Alicante, 03080 Alicante, Spain; ariquelme@ua.es (A.R.); roberto.tomas@ua.es (R.T.); joseluis.pastor@ua.es (J.L.P.); miguel.cano@ua.es (M.C.-G.)

* Correspondence: cconesa@um.es

Abstract

Sediment budgets and morphological channel adjustments are closely related to changes in stream power. In ephemeral channels, whose geomorphic response depends on the magnitude and frequency of discrete hydrological events isolated in time, such relationships are often difficult to establish. This study sought to quantitatively relate morphological adjustments to stream power along different reference channel reaches for the period 2018-2020 in the Azohía Rambla, a Mediterranean gravel-bed ephemeral stream in southeastern Spain. Very high resolution digital terrain models (VHRDTM), combined with ortophotographs and 3D point clouds, generated via SfM photogrammetry and terrestrial laser scanning (TLS) for pre- and post-event stages, together with ground-based surveys were used to estimate the spatial variability of morphological sediment budgets and to assess channel bed mobility and changes in net sediment flux during the study period in two spatial scenarios: reference channel reaches (RCRs) and pilot bed survey areas (PBSAs).The hydraulic variables (flow velocity, Froude number, shear stress, mean stream power and energy gradient, among other) were estimated using a 1D hydrodynamic model calibrated with field information.

The high resolution maps allowed a spatially-explicit analysis of stream power and transport efficiency in accordance with the areas of erosion and deposition in each RCR. The incision and bed armoring processes showed different trends according to the stream power (ω), cumulative excess energy (ε_c), and relative bed stability (RBS). The greatest morphological adjustments at the event scale coincided with ω values above 300 Wm^{-2}, ε_c higher than 3 MJ, and RBS below 0.5. The relationships between the mean stream power gradient at peak flood discharges and the changes in bed elevation verified the bed aggradation (an average surface raising of 0.17 to 0.22 m for δω/δs of -6.2 to -14.5 Wm^{-2}/m) during the major flood and bed scour (average surface lowering of 0.16 to 0.19 m for δω/δs of 5.8 to 10.6 Wm^{-2}/m)in the moderated events at the bankfull and sub-bankfull stages.

Key words: Stream power, morphological sediment budget, bedforms, SfM photogrammetry, terrestrial laser scanning, gravel-bed ephemeral channel, Southeastern Spain.

Introduction

Bed permeability and transmission losses, transport of mixed grain size materials, and especially the episodic and sudden nature of runoff events, are factors that make it quite difficult to get flow rates and assess morphodynamics in ephemeral gravel channels. In these streams sediment budgets and morphological channel adjustments depend on runoff, which is mainly controlled by the type of rainfall and the environmental conditions of the watershed area and the channel itself (Rojan et al., 2020). Particularly in arid and semiarid basins, they are settings for extreme morphological dynamics, associated with irregular and torrential peak flows, capable of reaching very high stream power values and sediment loads. The geomorphic response of these dry streams varies according to the magnitude and frequency of the flow events, which are especially sensitive to short-term climatic changes and human impacts (Segura-Beltrán and Sanchis-Ibor, 2013; Conesa-García et al., 2020a). The nature and impact of this response depend on the entity of each event, since larger and more energetic discharges mobilize and deposit a greater bed load, and minor events promote scouring and down-cutting phenomena (Pryor et al., 2014; Lotsari et al., 2018). The consequent effects vary from local bedform disturbances in low-flow stages to

overall channel adjustments after flash floods (Conesa-García et al., 1995; Benito et al., 2011; Norman et al., 2017).

Evaluation of the magnitude of geomorphic changes in ephemeral gravel-bed streams (EGBSs) is difficult because of the lack of gauging records, the permeability of the bed, abrupt variations in bedload, and their highly changeable hydromorphological dynamics. This explains why the literature on EGBSs is relatively scarce and requires more effort on empirical analysis and morphodynamic modeling (Bizzi and Lerner, 2015, Lotsari et al., 2018). In particular, the spatial and temporal morphological variability in EGBSs, as a function of variations in stream power, has been little studied (Levick et al., 2008; Ortega et al., 2014). Sutfin et al. (2014) proposed a non-metric multidimensional scale ordering, based on geometric and hydraulic variables: width-to-depth ratio (W/D), stream gradient (S), stream power (Ω),and shear stress (τ). Other authors related morphological adjustments in EGBSs to systematic changes in the mean stream power (ω) / resisting power (ω_c) ratio (ω/ω_c) (Bull, 1997), and hence in the transport efficiency, associated with the mean stream power gradient ($\partial\omega/\partial s$) and excess energy (Conesa-García et al., 2020b). Nor are there many studies aimed at evaluating these morphological changes in relation to erosion volumes, deposition, and sediment transport (sediment budgets) on a detailed scale. The multi-temporal application of very high resolution digital terrain models (VHRDTM) (pixel size <5 cm), generated using Structure-from-Motion Multi-View Stereo (SfM-MVS) from low-altitude unmanned aerial vehicles (UAV), has recently demonstrated its proficiency in the monitoring of submerged physical habitats of perennial and temporary streams (Woodget et al., 2019; Rowley et al. 2020; Salmela et al. 2020; Puig-Mengual et al., 2021) and morphological adjustments in dry channels (Calle et al., 2018; Flatley and Rutherfurd, 2018; Galea et al., 2019; Conesa-García et al., 2020a,b). Furthermore, this ability also extends to the detailed analysis of stream bed grain size and bedforms (Woodget and Austrums 2017; Vázquez-Tarrío et al. 2017) as well as rapid geomorphic changes, which affect the fluvial ecosystem dynamics (Rusnáket al., 2018). In addition, the 3D point clouds (3DPC) and VHR DTM, produced using terrestrial laser scanning (TLS), with a pixel size lower than 3 cm, offers higher performance to detect spatial differences in surface bed texture caused by specific events (Notebaert et al., 2009; Conesa-García et al., 2020a).

In this paper we propose an approach to assess, at the event scale, the relationships between sediment fluxes and stream power along an ephemeral gravel-bed channel, combining VHRDTM, provided by SfM-MVS and TLS, and a 1D hydrodynamic model

calibrated using field information. Specifically, there were two primary objectives: (1) to detect spatio-temporal patterns of sediment budgets and morphological adjustments along stream reaches with high bedload, and (2) to evaluate the relationships between changes in stream power and variations in erosion and deposition rates. These objectives were achieved in three steps: 1) the 3DPC datasets were used to test significant changes in height and volume after each event in reference channel reaches (RCRs) and pilot bed survey areas (PBSAs); 2) the results of hydraulic modeling during flash floods, including flow competence and bed stability indices, were analyzed at the cell scale; 3) erosion values, deposition, and net sediment flux were averaged for each budget cell from datasets of SfM and TLS; 4) the resulting maps of stream power, total volume difference average, and net thickness difference were combined to determine spatial relationships between these variables for each event. The work related to the first objective was focused on defining the spatial patterns of bed elevation changes, and associated processes of erosion and deposition, attributable to the magnitude of the flood or the combination of events. To test the second objective different hypotheses were examined:

(1) Spatial changes in ω values do not have a direct relationship with variations in bed stability associated with variable critical bed-shear stress and moving bed forms.

(2) The ω thresholds usually related to morphological changes in perennial gravel streams may differ from those required in unstable, ephemeral gravel-bed channels.

(3) The variability patterns of ω reflect the fluctuations in the flow velocity, shear stress, and Froude number.

(4) Greater changes in bed elevation and net sediment flux are mainly due to larger positive and negative values of the mean stream power gradient ($\partial\omega/\partial s$) and the $\omega/\omega c$ ratio.

(5) Sites with the greatest $\omega/\omega c$ ratios will have the highest values of cumulative excess energy per unit bed area (ε_c) and total sediment flux (T), which will promote bed scouring and vertical accretion processes. Conversely, locations where $\omega_c$equals or surpasses ωwill show the lowest ε_c and T, and the most stable bedforms.

2. Study area and environmental setting

This research was carried out in the Azohía Rambla, an EGBS draining a small coastal mountainous basin (13 km^2) in southeastern Spain (Region of Murcia). The study site is located in the Internal Zones of the eastern Betic Cordillera, so it takes part in the geological characteristics of its three major complexes (Nevado-Filábride, Alpujárride, and

Maláguide) (Egeler and Simon, 1969). The present-day contacts of these complexes are extensional detachments and low-angle normal faults. Metamorphic, poorly permeable materials (mainly phyllites, schists, and quartzites), of Permian and Triassic age, mainly appear in the headwater areas, while Quaternary detrital sediment and Miocene marls predominate in the alluvial fans and marginal zones of the valley bottom, respectively.

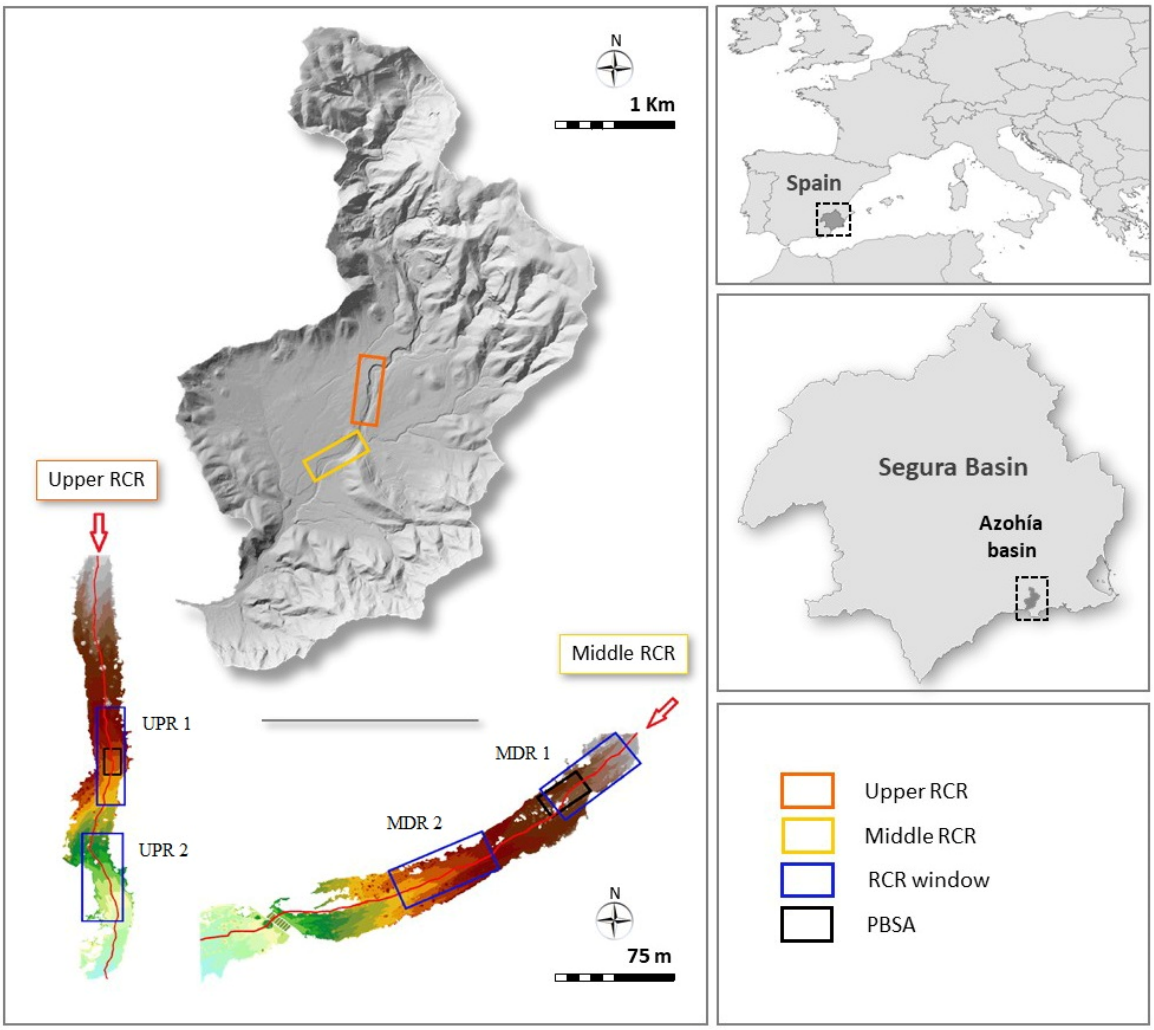

Figure 1. Location of the study area (Azohía Rambla basin) in southeastern Spain, and indication of the monitored channel reaches (upper and middle RCRs and their respective PBSAs).

Semiarid environmental conditions (precipitation of 310 mm/year, with a maximum 30-minute rainfall intensity above 50 mm h^{-1}, extreme droughts, and very high monthly potential evapotranspiration values (> 140 mm in the summer months) play a relevant role here in weathering and erosion processes. Added to this is scarce vegetation cover and

steep slopes, which often lead to large flash floods and intense fluvial geomorphic activity. A dense network of steep gullies in the headwaters area and detrital channel banks act as highly productive sources of sediment, especially coarse material (gravel and pebbles). As a result, the Rambla de la Azohía exhibits an active morphodynamics (rapid changes in bedform type and channel geometry). Two RCRs (the upper and middle RCR), c. 160 m in length, were chosen based on the accessibility and type of geomorphic adjustment. These stream stretches better represent the changes in stream power and their relationships with the variations in net sediment fluxes and bedforms. In contrast, in the lower reach, global changes are the product of sediment-laden floodwater spills, affecting crevasse splays and a wide, active flood bed, making it difficult to apply this approach (Ali and De Boer, 2003).

3. Material and methods

VHRDTM derived from UAV-SfM, Global Navigation Satellite System (GNSS) data, and TLS were used to determine sediment budgets and changes in bed elevation in pre- and post-event stages and to establish the topographic base before each flash flood. In both RCRs, erosion and deposition areas and volumes were obtained at the pixel level for each event, while at the cell scale morphological sediment budgets and net sediment fluxes were averaged. The hydraulic datasets were obtained from the application of a 1D hydrodynamic model fed by theoretical hydrographs, previously calibrated and validated with direct water measurements during the runoff, made using pressure sensors. Using a GIS to integrate all this information, spatial sediment budgets and stream power values were mapped and their relationships were calculated under different balances (negative or positive) between ω and ω_c for each pair of consecutive cells. Seven significant rainfall events (>35 mm/day) occurred in the analysis period (September 18, 2018 to January 9, 2021), but only three of them generated peak discharges capable of causing perceptible geomorphic effects: a larger one, characterised by a bank overtopping discharge (flash flood of 19–20 April 2019), and two other moderate peak discharges at bankfull and sub-bankfull stages, the peak flow of 24 March 2020, and 12 September 2019, respectively (Table 1).

Table 1.Dates of occurrence of flow events and field surveys using UAV-SfM and/or TLS techniques, with indication of rainfall data and peak discharges for each channel reach.

Event/ fieldsurvey	Date	P (mm)	Rainfallduration (h)	I1h (mm h^{-1})	I30' (mm h^{-1})	Qp (m^3 s^{-1})		
						UPR	MDR	LWR
UAV-SfM	18 September, 2018							
Peakflow	18 November, 2018	35.6	9.3	17.6	32.4	0.1	0.1	0.2
TLS	29 November, 2018							
Peakflow	19-20 April, 2019	123.2	21.2	37.3	46.0	21.9	31.3	46.1
UAV-SfM/TLS	5 September, 2019							
Peakflow	12 September, 2019	93.9	16.9	20.2	26.4	8.4	10.9	15.1
Peakflow	2 December, 2019	59.3	20.3	9.8	17.8	1.2	1.7	2.9
TLS	16 January, 2020							
PeakFlow	20 January, 2020	66.3	20.8	10.6	12.8	2.7	3.6	5
Peakflow	23-24 March, 2020	119.3	34.2	22.9	28.8	11,6	15,4	20,8
UAV-SfM/TLS	26 July, 2020							
Peakflow	9 January, 2021	41.0	34.0	2.7	-	0.3	0.4	0.8

P = precipitation (mm); Qp = peak discharge (m^3 s^{-1}); I1h = rainfall intensity (mm h^{-1}); I30' = maximum 30-minute rainfall intensity (mm h^{-1}); UPR = upper channel reach; MDR = middle reach; and LWR = lower reach.

Specifically, five follow-up stages resulted from the combination of the two techniques. Two of them were covered by SfM data: 1) September 2018 to September 2019, including the events of November 18, 2018 and April 19-20, 2019, and 2) September 2019 to July 2020, during which four moderate or low peak flows occurred. The other three survey periods were defined from the TLS surveys: 3) December 2018 to September 2019, including only the flash flood from April 19 to 20, 2019, 4) September 2019 to January 2020, in which the flood of September 12-13, 2019, was the key event, and 5) January 2020 to July 2020, which monitored the peak flow on March 24, 2020. Changes in morphological sediment budgets were quantified for all stages using channel-bed pixels extracted from the two types of VHR MDT. However, relationships between stream power variables and changes in bed elevation and bedload sediment mass balance at the event scale could only be analyzed with the pre and post-event TLS surveys.

3.1. Changes in ground elevation and sediment budgets derived from VHR MDT datasets

Changes in bed elevation, areas and volumes of erosion and deposition, and sediment fluxes (net -ΔV- and total -T- flux) were calculated for both RCRs (upper -UPR- and middle -MDR- stretches) using VHR MDT and high-density 3DPC, generated from the

SfM-MVS and TLS surveys. In particular, average difference in total volume, net thickness difference, total area of surface lowering and raising, and percent imbalance (departure from equilibrium), among other variables, were provided by both techniques for the two RCRs. Comparison of each pair of successive high resolution images at the pixel level (2-3 cm pixel size) yielded very good accuracy in the calculation of sediment budgets based on the monitored events. The errors associated with these estimates were described and assumed for each comparative survey analysis, according to Brasington et al. (2003). The areas with the highest density 3DPC (PSBAs) were used to monitor modifications of the detail in the bedforms.

3.1.1. SfM-MVS photogrammetry

The selected channel stretches and adjacent areas were surveyed using a Phantom 4 Pro, with a 20-Mp camera and 1-inch sensor, at an average flight height of 50 m, in order to gain very high resolution aerial images (≈ 1-2 cm resolution). The flight track and common parameters were pre-programmed for the software tool DJI GS Pro© for all the surveys. Ground Control Points (GCPs) and Check Points (CPs) were established in the field, using coded targets printed from Agisoft PhotoScan Pro 1.2.2 © software (Agisoft, Russia). In each of the surveys, approximately 66 % of the measured points corresponded to GCPs, for geo-referencing purposes, and the remainder corresponded to CPs for the validation of the VHRDTM (Conesa et al., 2020a; Puig-Mengual et al., 2021). The topographic survey of the coded marks was carried out by a GPS-RTK Prexiso G5 © station (Leica, Germany), connected via a mobile signal to the regional network of differential corrections, GPS GNSS (Network of Reference Stations in the Region of Murcia "Meristemum"). Among these points, some were permanently marked with FENO survey markers. All field support points were measured in the WGS84 global reference system.

In order to ensure the correct definition of homologous points between images, consistent overlaps of 80 to 90% were applied (Seifert et al. 2019). The captured images, the GCPs, and the CPs were used in the Agisoft PhotoScan Pro v.1.2.2© (Agisoft, Russia) structure-from-motion photogrammetry software, which allowed the generation of point clouds, a continuous textured mesh, VHR DTM (pixel size 0.02 m), and an orthomosaic (Conesa et al., 2020a; Puig-Mengual et al., 2021). These final products were geo-referenced in a global system (WGS84) for further analysis. The digital elevation model of the topographic difference (DoD) between the UAVs-collected VHR DTM in different field

surveys, as well as between the TLS-generated VHR DTM, was developed in ArcGis 10.5 © (ESRI, USA), by subtraction of the final topography from the previous one for the same area (Wheaton et al., 2010). The extraction mask for the water sheet at different peak flows in each RCR was applied to all the DoDs, thus enabling the precise comparison of the morphological channel changes and sediment budgets associated with each event.

3.1.2. Terrestrial Laser Scanning (TLS)

A Leica ScanStation C10 model terrestrial 3D laser scanner was used to get a high resolution sediment budget. This scanner captures point cloud geometrical information at a velocity of 50,000 points per second at a distance of up to 300 m, with a precision of 2 mm. This information was combined with high resolution and high quality 2D RGB true color camera information. Multiple overlapped scans were performed from different benchmarks intentionally selected along the channel bed to cover the total area of interest for a detailed geometrical definition. The output 3D point clouds (3DPC) were then registered, using HDS targets from the dataset of September 5th, 2019 as the master 3DPC for all the TLS scans. On this date a field survey was jointly carried out with SfM-MVS, using FENO survey marks as the common reference for both techniques, TLS and UAV-derived 3DPC. The scans performed in November 2018, January 2020, and June 2020 were registered at that benchmark, with a mean error of 2 mm, using the iterative closest point (ICP) plugin of CloudCompare software and some stable nearby buildings as reference points. Then, the differences in elevation and the volume changes after each flow event were calculated for both pilot bed survey areas (PBSAs), one within the upper RCR (8.55 x 17.7 m) and the second in the middle RCR (16.3 x 27.55 m). The vegetation, mainly composed of scrubs and shrubs, was removed using the CANUPO CloudCompare plugin (Brodu and Lague, 2012; Girardeau-Montaut, 2020; Lague et al., 2013). Subsequently, the 3DPC data captured for the different dates were rasterized, resulting in a 5-cm grid, and were interpolated for those pixels in which no TLS information was available. Figure 2 shows the steps taken to reach the rasterized 3D point cloud, once the vegetation cover had been removed.

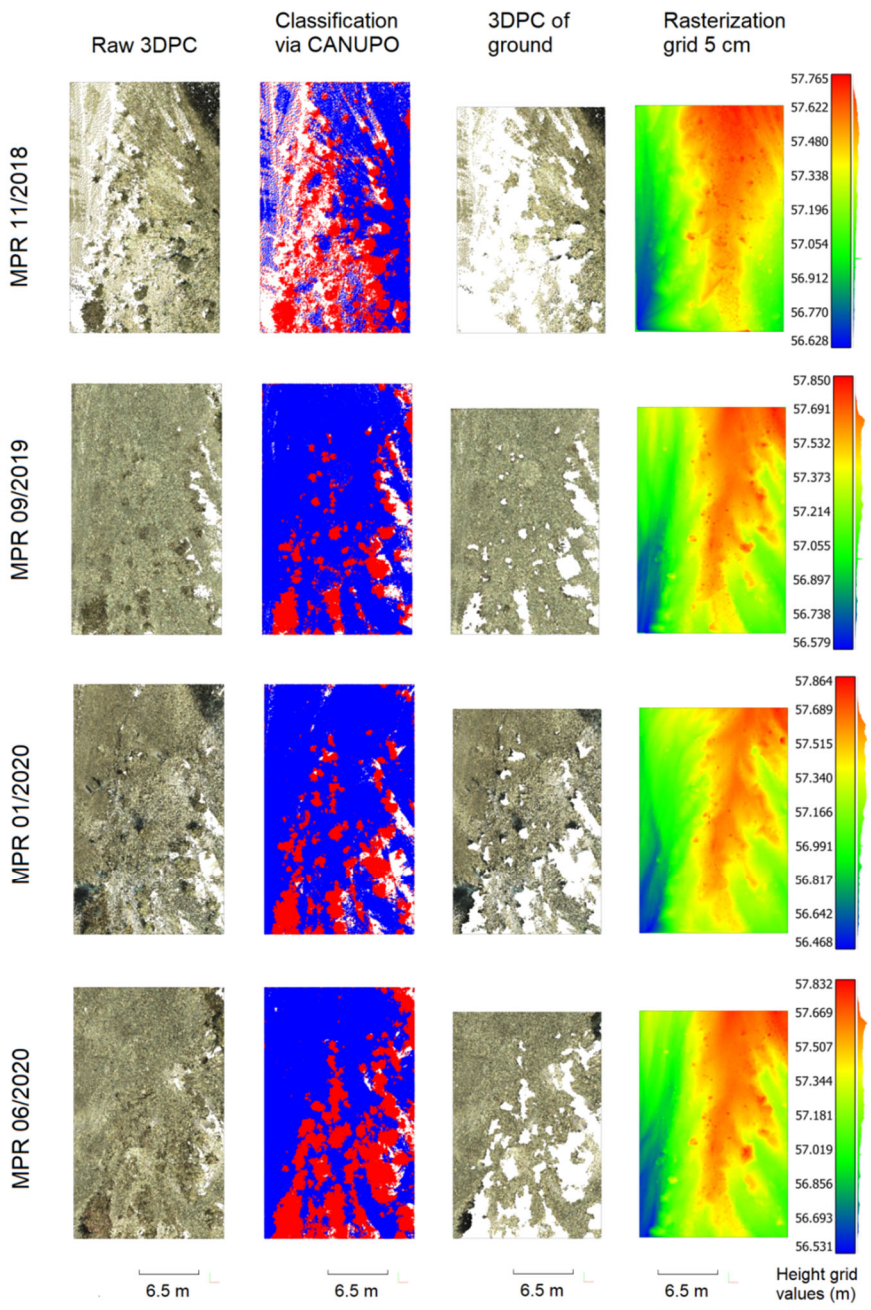

Figure 2. Rasterization process for the MPR presented as a grid. Each row corresponds to a scan and the labels show the respective dates. The first column shows the raw 3DPC, the second the classification using CANUPO (Lague et al., 2013), the third the extraction of the ground points, and the fourth the rasterized 3DPC.

3.1.3. Morphological sediment budgets at the cell scale

Areas of erosion and deposition were quantified by comparing each pair of successive VHR DTM and high-density 3DPC generated from SfM-MVS and TLS surveys,

respectively. The resulting bed elevation change maps were used to determine sediment budgets within a series of 212 budget cells with a lateral extent defined by the union of the water sheet polygons for each flood event and a downstream length of 2.5-3.0 m. Average bed elevation differences were calculated for each budget cell from all the pixel values in that cell. Net sediment fluxes (ΔV) were given for each budget cell and for the entire 160 m upper and middle RCRs by expressing negative (bed scouring) or positive (vertical accretion) differences in bed elevation, while total sediment flux (T) was calculated as the sum of gross erosion (E) and gross deposition (D).

3.2. Rainfall-runoff method and hydraulic modeling

Hydrographs were estimated using a rainfall-runoff model, at the beginning of each RCR, for the flood events that occurred during the analysis period (2018-2021). Field indicators, such as evidence of high-water marks (HWM), and water levels measured by pressure sensors (Levelogger Edge LT and Baralogger Edge) were used to test and calibrate the hydrograph data for each event. The most common HWM found were vegetation debris, which may be close to the water level during peak flow. In addition, pressure level sensors (PLS) were placed between both RCRs. The barometric compensation was automatically performed, so the delay to compensate for the fluctuations in atmospheric pressure recorded by the levelogger was minimal, leading to accurate water level data. The SCS dimensionless unit hydrograph (U.S. Soil Conservation Service, 1972) was calculated for the soil moisture conditions before rainfall-produced floods and from hyetograph data for intervals of 5 minutes at the Cuesta del Cedacero station. By combining the HEC-HMS 3.5 program, the HEC-GeoHMS 1.1 of ArcView 3.x, and a DTM with a grid resolution of 4 × 4 m (Project Natmur, 2008),we generated the drainage networks and watersheet area. As the main hydrological abstraction, the infiltration curve number (NC) of each sub-basin was used. Maps were drawn up in a GIS environment to define soil types, vegetation, and slopes, using the lithological layer in vector format from the Geological and Mining Institute of Spain (IGME) (1:50,000), soil mapping of the LUCDEME project (1:100,000), Corine Land Cover maps (CLC2012), and 1:5,000 orthophotographs.

The peak discharge data were then transferred to the 1D hydrodynamic model HEC-RAS (USACE, 2016), supported by VHR DTM, in order to get the flow cross-sections, channel profiles, water sheet limits, and hydraulic variable datasets. A total of 100 cross-sections were drawn in the upper RCR and 112 in the middle RCR, with an average separation of

2.0-3.5 m between them, for subcritical flow regimes. The results obtained in the calibration and validation events were evaluated using the Nash-Sutcliffe efficiency (NS) and percent bias (PBIAS). The respective values of NS and PBIAS were 0.86 and 7.81% in the calibration period and 0.81 and -4.1% in the validation events.

3.3. Mapping spatial changes in stream power during peak discharges

The peak discharges used to calculate stream power along the RCRs included a major flash flood (19-20 April, 2019) and two moderate flow events (12-13 September, 2019 and 24 March, 2020), all having different geomorphic impacts. For each cross-sectional flow area, information was obtained about the hydraulic radius (R), velocity (υ), Froude number (Fr), shear stress (τ), and stream power. Power per unit length of stream (Ω) and mean stream power (ω) at peak flood discharge (Q_p) were calculated according to Eqs. 1 and 2, respectively (Leopold et al., 1964).

$$\Omega = \gamma Q S_w \quad (1)$$

$$\omega = \Omega / w \quad (2)$$

where γ is the specific weight of water (Nm^{-3}), Q is peak discharge (m^3/s), S_w is the water surface slope (m/m), which is used to estimate the energy gradient, and w is the water-surface width (m). Ω represents the energy dissipation per unit channel length and ω the energy expenditure per unit bed area. The width, average depth, and maximum water depth for each cross-section and its corresponding raster cell were acquired from the cross-sectional polygons of flow. The stream power values extracted by cross-section were averaged by budget cell level (i.e. ω) to compare with the sediment budgets at the same scale (Figure 3). For this purpose, a spatial interpolation of the values obtained in the consecutive cross-section pairs (Conesa García *et al.*, 2020b) was performed, resulting in raster maps with cells of similar size to those got for the calculation of sediment budget.
The mean stream power gradient (∂ω/∂s) was calculated by subtracting ω in cross-sectional cell i from the average ω in cells i−1 to i-3 and dividing the difference by the distance between the centroids of the extreme cells in each set of consecutive four budget cells along the channel centerline. This distance was normally around 10 m, as each cell is 2.5-3.0 m long. Positive and negative ∂ω/∂s values show downstream increases and decreases in ω, respectively (Lea and Legleiter, 2016).The parentheses refer to the location of a given cell (for example, ω in cell i would be expressed as ω (i)).

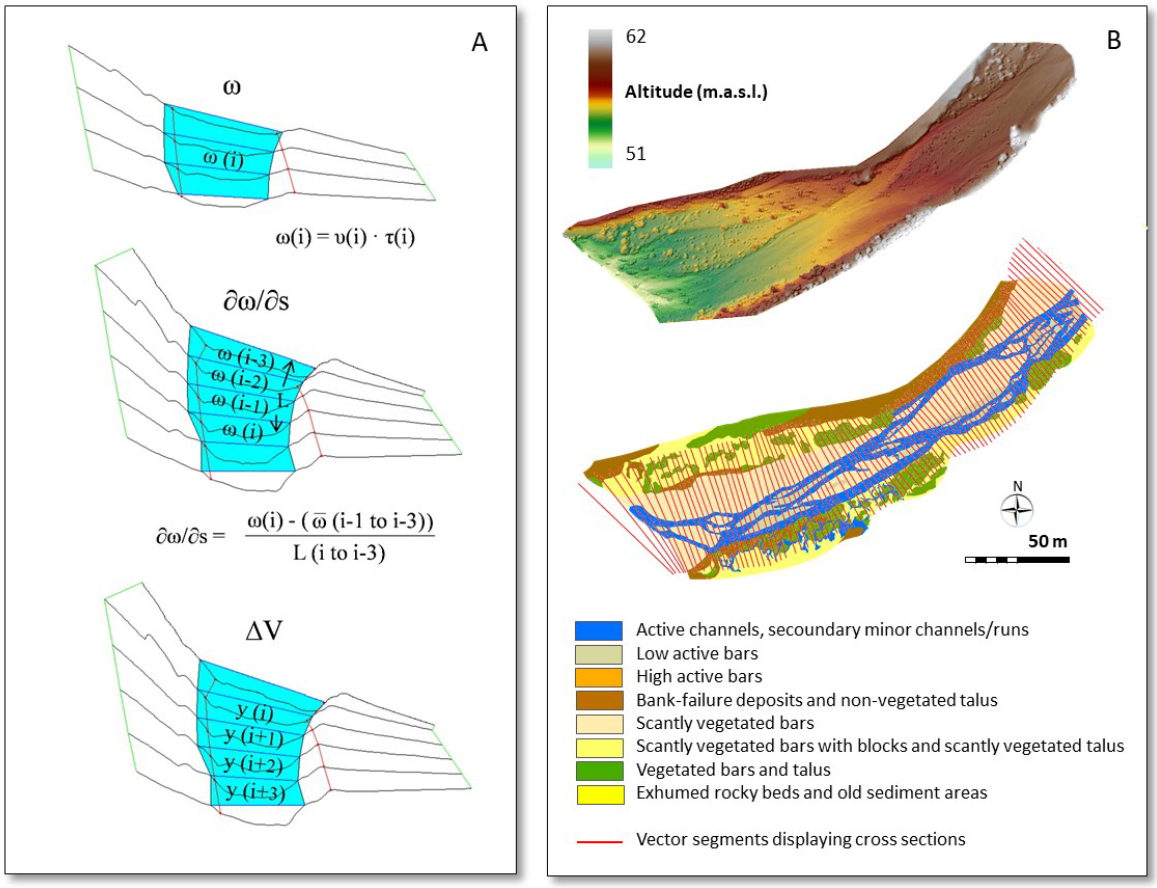

Figure 3. (A) Diagram of budget cells showing how ω, $\partial\omega/\partial s$ and ΔV were estimated. (B) VH DTM (at the top), and raster layer (at the bottom) showing bedforms within the peak flow limits; red vector segments display cross-sections for which BFS_{pf} was calculated.

The energy expended beyond the critical mean stream power (ω_c) and the ω/ω_c ratio in each cross-sectional cell were also estimated to assess the spatial distribution of energy available for sediment transport and morphological bed changes during peak flows. The excess energy per unit bed area (ε) expended above ω_c in these stages was determined by calculating ω from each peak discharge (Q_{pf}) and comparing the values to ω_c obtained using Eqs. (10) and (16) from Parker et al. (2011), which calculate ω_c as a function of slope and grain size. The bed slope was extracted from the VHR DTM described above. Volumetric grain-size sampling was performed for representative cross-sections in each RCR, differentiating the armored surface layer and the subsurface material. The median grain size (D_{50}) and the 84th percentile (D_{84}) were calculated for both layers in different bedforms within each cross-section. For the events in which ω was greater than ω_c, the difference between ω and ω_c was multiplied by the number of seconds that elapsed while the maximum flow lasted, in order to get the excess energy accumulated per unit area of the bed (ε_c), in joules. Finally, the ε_c values were related to ΔV and total flux (T).

3.4. Relative bed stability indices and transport efficiency

The transport efficiency in this EGBS was tested by combining two substrate stability indices: 1) the "Relative Bed Stability" (RBS), and 2) the "Bed-form Stability" (BFS). We adopted the RBS index from Olsen et al. (1997), defined as the ratio between the critical bed shear stress required to mobilize the D_{84} size particle (τ_{c84}) and the shear stress reached in each flow peak (τ_0) (Eq. 3).

$$RBS = \tau_{c84}/\tau_0 \quad (3)$$

$$\tau_{c84} = \tau_c^*(\rho_s - \rho)gD_{84} \quad (4)$$

where ρ_s and ρ represent the sediment and water densities, respectively, g is the acceleration due to gravity, and τ_c^* is the critical value of the dimensionless Shields parameter. Finally, the shear stress for the discharge peak in each flow event was estimated as:

$$\tau_0 = \rho gRS \quad (5)$$

where R is the hydraulic radius and S is the water surface slope. If RBS is greater than 1, the bed is presumed to be fully mobilized only for peak discharges larger than that considered and the channel bed is relatively stable under such conditions. Conversely, if RBS is less than 1, the bed is mobilized at the sub-peak flow stage and the bed is presumed to be unstable, the transport efficiency increasing as the index approaches 0.

The BFS index, described by Conesa-García et al. (2020b), defines the relative stability of the bed forms according to the particle grain-sizes, vegetation cover, and height on the bed; for peak flow events(BFS_{pf}), it was calculated using Eq. 6.

$$BFS_{pf\,(i)} = \left[\left(\sum vr_{bgu(i)} \cdot w_{bgu\,(i)}\right)/W_{pf\,(i)}\right]/n_{bgu\,(i)} \quad (6)$$

where vr_{bgu} is the value assigned to each type of bed geomorphic unit (bgu), depending on its resistance to erosion observed in recent torrential flows, w_{bgu} is the width of each bgu in a channel cross-section, W_{fp} is the flow width, and n_{bgu} is the number of bgu. In our case, the maximum n_{bgu} = 8, with the corresponding values of vr_{bgu}, as follows (from samller to larger resistance): 1. Active channels, secondary minor channels/runs, pools, and gully beds; 2. Low active bars; 3. High active bars; 4. Bank-failure deposits and non-vegetated talus; 5. Scantly vegetated bars; 6. Scantly vegetated bars with blocks and

scantly vegetated talus; 7. Vegetated bars and talus; 8. Exhumed rocky beds (substrate outcrops) and old sediment areas (rock blocks and cohesive bars) (Figure 3). Such classes were extracted from the bgu affected by each peak flow. This index varies between 0 and 1, and the value of 0.5 is a threshold that discriminates in relative terms between stable ($BFS_{pf} > 0.5$) and unstable bed forms.

3.5.Relationships of stream power with sediment budget and bed stability

Values of the volumes of erosion (EV) and deposition (DV), net volume fluxes (ΔV), and elevation differences (Δe) averaged for each budget cell i, from high resolution data of UAV-SfM and TLS, were got along the two RCRs and for the time intervals under study.
The mean stream power gradients at cell i for the budget cells meeting thecriteria in Table 2 were compared to the E and D values at the same cell and to the ΔV volumes at cells i through i + 3 downstream.
Cross-correlation between $\partial\omega/\partial s$ and the net sediment flux at cell i + j was used as described by Lea and Legleiter (2016) to assess the spatial relationship between changes in stream power and transfers of sediment downstream. According to these criteria, it is assumed that only budget cells with ω greater than ω_c can experience sediment transport at the peak flow stage, the bedload being negligible in cells with a ω/ωc ratio lower than 1. We included in the cross-correlation analysis four conditions, which are described in Table 2, and we discarded those that implied the premise of ω_c being greater than ω.

Table 2. Cases considered for the comparison of $\partial\omega/\partial s(i)$ and $\varepsilon_c(i)$ with $\Delta V(i+j)$ and $T(i+j)$ in each flood event and the hypothesized geomorphic trend in budget cell i or downstream budget cells i+j, according to Lea and Legleiter (2016).

Case	Description	Hypothesizedgeomorphictrend	% UPR	% MDR
1: ω(i) > ω(i − 1) >ωc	ω increases downstream and exceeds ωc for both budget cells	Erosion	46.2	23.3
2: ω(i) >ωc> ω(i − 1)	ω increases downstream and exceeds ωc in cell i	Minorerosion	0.0	11.7
3: ω(i − 1)> ω(i) >ωc	ω decreases downstream but exceeds ωc for both budget cells	Minordeposition	52.3	55.0
4: ω(i − 1) >ωc> ω(i)	ω decreases downstream and falls below ωc in cell i	Deposition	1.5	10.0

The percentages refer to the frequency of each case in the upper and middle RCRs for the flow peak of 19-20 April, 2019.

Hypotheses (1) and (2) were tested by using scatter plots to relate $\partial\omega/\partial s(i)$ to E(i), D(i), and ΔV(i + 1 to 3). By interpreting these scatter plots, the effect of the downstream spatial

lag on the relationship between ∂ω/∂s and sediment flux was evaluated. Furthermore, the excess accumulated energy per unit area of the bed, εc (i), was plotted against the total accumulated flux (T) to examine hypothesis (3), that there is a positive correlation between these two variables.

3.6. Assessment of bed elevation profiles using channel central and lateral lines

To assess changes in bed elevation a comparison of the longitudinal and transverse channel profiles was performed throughout the two RCRs and PBSAs. Specifically, three longitudinal profiles derived from SfM data and four from TLS surveys during the November 2018 to July 2020 period were compared. Perpendicular to these profiles, three transverse profiles were delineated for each survey date: one central and two at the end of both RCRs and PBSAs. We first obtained the channel centerline (CL) from the flow sheet boundary lines, using the method described by Golly and Turowski (2017). In order to define patterns of lateral bed change regarding the central channel axis, two lateral lines (one separated from the centerline by 3 m in the upper RCR and one separated by 1.5 m in the middle RCR) were drawn: one to the right (RL) and another to the left (LL). From the centerlines and lateral lines, their bed elevation difference values (Δe) were extracted after each of the main study events (April 19, 2019, September 12, 2019, and March 24, 2020). To eliminate the effect of the surface roughness of gravel and pebbles, the pixel values were averaged in 20-cm length intervals. The relationships of Δe CL with Δe RL and Δe LL were plotted. In addition, scatter plots comparing the differences in Δe RL and Δe LL with respect to Δe CL according to downstream distance were displayed for the bed sites with higher density of points and less distortion in the elevation values. The elevation variation patterns thus detected will reflect differential changes in bedload transport and channel bed morphology (e.g. the downstream cross-sectional balance between erosion and deposition) (Kasprak et al., 2015). This is particularly relevant in ephemeral channels, where bed elevation often appears to remain unchanged after a bedload-transporting flow event (Singer and Michaelides, 2014).

4. Results and discussion

4.1. Morphological sediment budgets at very high spatial resolution

The DoDs derived from each successive VHR DTM pair made it possible to evaluate very precisely the changes in bed elevation and sediment budget caused by a single isolated flash flood or two or more events of different magnitude. Specifically, in the RCRs studied here, the SfM-MVS data showed very different sediment budget patterns, associated with the magnitude of the monitored events. During the first stage (September 2018–September 2019) the upper RCR functioned as a sink for coarse sediments due to high instantaneous bedload fluxes at the peak flows on November 18, 2018 and April 19-20, 2019, while the middle RCR experienced channel deepening and bar accretion. As a result, the greatest deposition thickness was found in pre-existing alluvial bars (Figure 4). In the second period (September 5, 2019 to July 26, 2020), during which two moderate events and two others of very low flow occurred, superficial bed washing and scouring predominated, causing a general surface lowering.

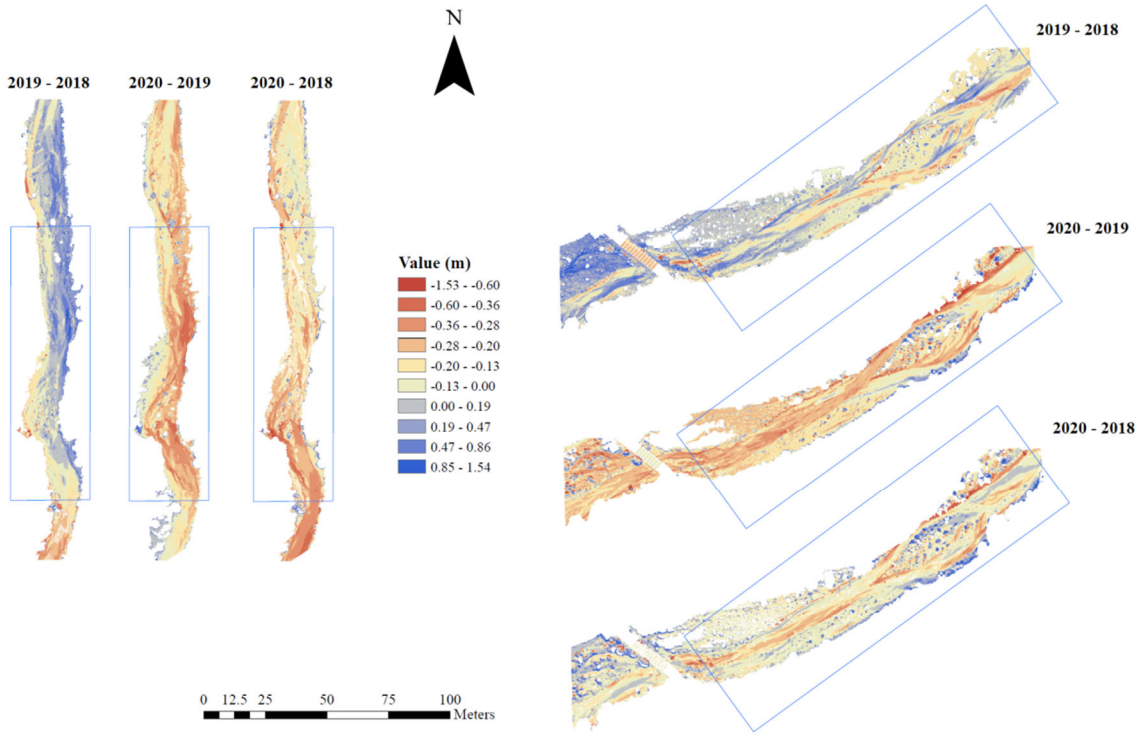

Figure 4. DEMs of difference (DoDs) for the upper and middle RCRs, using VHR DTM derived from SfM-MVS, for the periods from September 18, 2018 to September 5, 2019, from September 5, 2019 to July 26, 2020, and the two consecutive periods together (2018-2020).

Table 3 shows significant cumulative changes in ground surface elevation for both periods. For the upper and middle reaches, the average net thickness differences were, respectively, +22 and +21 cm in the first stage and -19 and -16 cm in the second. The DoDs of these two

periods revealed a higher average deposition rate in the middle reach (UVSR = 0.218 m^3 m^{-2} and 0.317 m^3 m^{-2}, respectively) than that of the upstream erosion (UVSL = 0.128 m^3 m^{-2} and 0.229 m^3 m^{-2}, respectively). This suggests that the sources of sediments included not only the upper RCR but also gullies close to the headwater area and intermediate channel sections between the two RCRs, where bank breaking and gravel bar removal are especially active processes (Conesa et al., 2020a). Regarding the Total Net Volume Difference of both DoDs, the increase in net deposition was 2.26 % for the upper RCR and 31.13 % for the middle RCR.

Table 3. Statistical descriptors relating to the morphological sediment budgets calculated for the overall channel reach (OVR) and reference channel reaches (RCRs) in the UPR and MDR for the period September 2018 to July 2020 (SfM data).

Statistic		TAI	TNVD		ANTD		PI	TASL	TASR	UVSL		UVSR		SD *
Channel Reach Type		m^2	m^3	% Error	m	% Error	% Value	m^2	m^2	m^3 m^{-2}	% Error	m^3 m^{-2}	% Error	m
PeriodSeptember 2018 to September 2019														
UPR	OVR	4657	958	0.044	0.206	0.044	0.470	372	4285	0.083	0.107	0.231	0.043	0.137
	RCR	2763	613	0.044	0.222	0.044	0.486	67	2695	0.128	0.070	0.231	0.043	0.118
MDR	OVR	8720	2092	0.040	0.240	0.040	0.489	234	8486	0.103	0.086	0.249	0.040	0.121
	RCR	4885	1013	0.046	0.207	0.046	0.486	168	4717	0.086	0.102	0.218	0.046	0.106
PeriodSeptember 2019 to July 2020														
UPR	OVR	4887	-830	-0.053	-0.170	-0.053	-0.400	4430	457	0.211	0.047	0.225	0.042	0.171
	RCR	2976	-575	-0.048	-0.193	-0.048	-0.420	2744	232	0.229	0.043	0.237	0.040	0.162
MDR	OVR	7795	-1318	-0.051	-0.169	-0.051	-0.331	6728	1068	0.246	0.040	0.314	0.031	0.256
	RCR	4707	-742	-0.055	-0.158	-0.055	-0.319	4044	663	0.235	0.042	0.317	0.030	0.243
PeriodSeptember 2018 to July 2020														
UPR	OVR	4614	93	0.074	0.020	0.070	0.091	2193	2421	0.095	0.068	0.125	0.066	0.185
	RCR	2750	13	0.072	0.010	0.071	0.024	1466	1284	0.087	0.066	0.110	0.067	0.173
MDR	OVR	8553	637	0.090	0.074	0.090	0.219	3365	5188	0.121	0.076	0.201	0.047	0.273
	RCR	4805	231	0.072	0.048	0.071	0.152	2142	2663	0.124	0.076	0.186	0.051	0.252

TAI = Total Area of Interest (m^2); TNVD =Total Net Volume Difference (m^3); ANTD =Average Net Thickness Difference (m) for the Area of Interest; PI =Percent Imbalance (departure from equilibrium); TASL =Total Area of Surface Lowering (m^2); TASR =Total Area of Surface Raising (m^2); UVSL = Average Unit Volume of Surface Lowering (m^3 m^{-2}); UVSR = Average Unit Volume of Surface Raising (m^3 m^{-2}); SD* =Standard Deviation of the Net Thickness Differences (m); UPR = Upper reach; MDR = Middle reach; OVR = Overall channel reach; RCR = Reference channel reach.

The TLS data provided further information on changes in source-to-sink sediment transfer at the event scale. In particular, morphological sediment budgets in the RCRs and PBSAs were calculated using DoDs for the studied peak events. The PBSAs offered the best results, as they were defined by higher density 3-D point clouds (Fig. 5). In these areas, the major event produced a positive generalized sediment budget, with an average unit volume

of 21.55 dm^3 m^{-2} in the upper PBAS and 10.03 dm^3 m^{-2} in the middle PBAS. The two moderate flow events had different behavior patterns: the bankfull discharge caused the highest incision rates in the upper PBAS, with an average unit lowering volume above 90 dm^3 m^{-2}, and the largest deposition in the middle PBAS, where the average unit volume of surface raising was 51.9 dm^3 m^{-2}. By contrast, at the sub-bankfull stage more moderate vertical erosion and bed lowering predominated along both channel stretches.

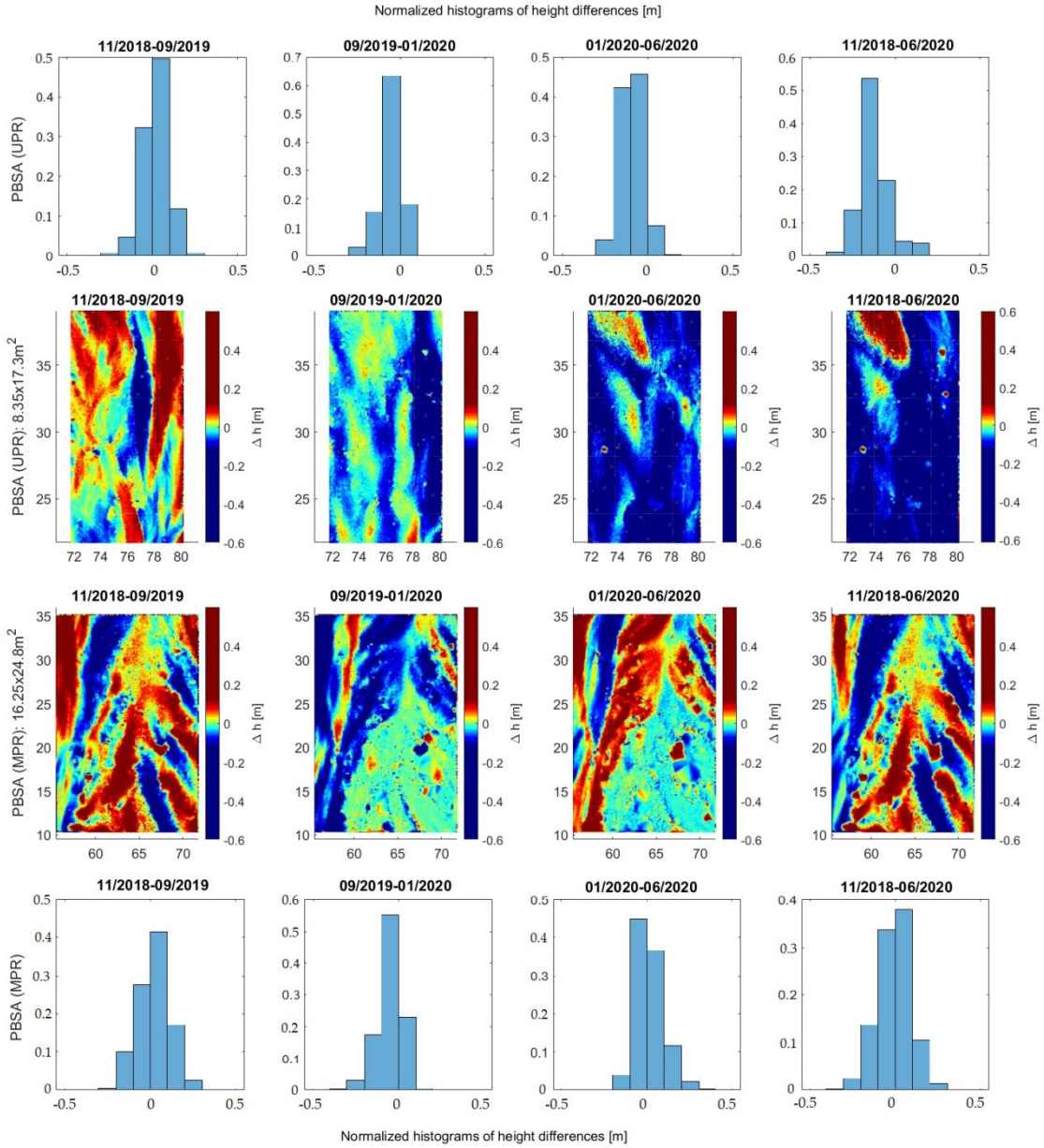

Figure 5. DEMs of difference (DoDs) and normalized histograms of the height differences for the upper and middle PBSAs, comparing the 2018, 2019, and 2020 3DPCs, based on the TLS survey. They display the sediment budget primarily attributable to the peak flow events of (a) 19-20 April, 2019, (b) 12 September, 2019, (c) 24 March, 2020, and (d) the whole analysis period (November 2018 to July 2020).

The analysis of budgets expressed in unit volume for 10-cm elevation intervals shows that the more extensive morphological adjustments coincided with the largest volumetric variations, the bed elevation ranging between −0.2 and +0.2 m (Table 4). Within these intervals, the greatest unit volumes of deposition (86.1dm^3 m^{-2}) and erosion (83.2 dm^3 m^{-2}) were recorded in the middle and upper PBSA, respectively, during the bankfull discharge of March 2020. These results suggest that effective discharge for bed load transport occurs at higher water stages and greater recurrence intervals than bankfull discharge, which is consistent with the cases studied by Emmett et al. (2001) and Gomez et al. (2007). In both RCRs the channel width is constrained by the stability of the bank material and its resistance to erosion during flows at or near the bankfull stage, which also scour the bed. In addition, constraints on the mobility of bed material, due to channel armoring processes, mean that a higher peak discharge is required to transport the greatest amount of bedload. The budgets at the cell level reflected the same erosion-deposition patterns and relationships between channel reaches as at the pixel resolution.

Table 4. Changes in unit volume (dm^3 m^{-2}) and total mean volume per budget cell (dm^3), got for elevation intervals of 10 cm, and global height differences (Δe) in each pilot bed survey area (PBSA), based on TLS datasets covering the periods November 2018 to September 2019[1], September 2019 to January 2020[2], and January 2020 to July 2020[3].

	Unit volume (dm^{3}m^{-2})						Total mean volume per budget cell (dm^3)					
	PBSA (UPR)			PBSA (MDR)			PBSA (UPR)			PBSA (MDR)		
Δe (m)	2018 2019[1]	2019 2020[2]	2020 2020[3]	2018 2019[1]	2019 2020[2]	2020 2020[3]	2018 2019[1]	2019 2020[2]	2020 2020[3]	2018 2019[1]	2019 2020[2]	2020 2020[3]
-0.5/-0.4	-0.05	-0.15	-0.64	-3.59	-0.15	-0.39	-1.9	-5.3	-10.4	-312.7	-10.0	-10.5
-0.4/-0.3	0.00	-0.21	-0.17	-2.46	-0.02	-0.13	0.0	-7.4	-57.3	-214.1	-1.3	-3.5
-0.3/-0.2	-1.47	-7.67	-8.76	-3.86	-0.23	-0.10	-59.4	-270.0	-507.5	-335.7	-15.8	-2.8
-0.2/-0.1	-6.60	-22.54	-56.53	-16.14	-9.35	-14.65	-266.0	-793.6	-1281.7	-1405.4	-631.2	-398.5
-0.1/0	-11.32	-26.36	-26.69	-11.35	-23.91	-36.49	-456.4	-928.4	-222.6	-987.7	-1613.6	-992.4
ΔV<0	-19.44	-56.93	-92.79	-37.40	-33.66	-51.76	-783.7	-2004.7	-2079.5	-3255.6	-2271.9	-1407.7
0/0.1	21.80	2.68	2.30	18.52	3.09	43.04	878.9	94.3	31.7	1612.5	208.7	1170.6
0.1/0.2	17.38	0.05	0.28	22.84	1.14	43.12	700.7	1.6	78.0	1988.9	76.7	1172.9
0.2/0.3	1.38	0.01	0.02	4.67	0.79	13.31	55.6	0.3	4.5	406.3	53.6	362.0
0.3/0.4	0.16	0.01	0.01	0.57	0.70	2.52	6.3	0.2	0.1	49.3	46.9	68.6
0.4/0.5	0.27	0.07	0.08	0.83	1.69	1.66	10.9	2.5	0.6	72.0	114.4	45.1
ΔV>0	40.99	2.82	2.69	47.43	7.41	103.65	1652.4	98.9	115.0	4129.0	500.3	2819.2
ΔV	21.55	-54.12	-90.10	10.03	-26.25	51.89	868.7	-1905.8	-1964.6	873.4	-1771.6	1411.5

Table 4 also provides the total mean volumes per budget cell for the two PBSAs in each time interval. For the entire analysis period, erosion exceeded deposition, resulting in a

final positive net sediment flux. From the net sediment flux volumes in each budget cell, the height of scour and fill were obtained for the three survey stages and the two RCRs (Figure 6).

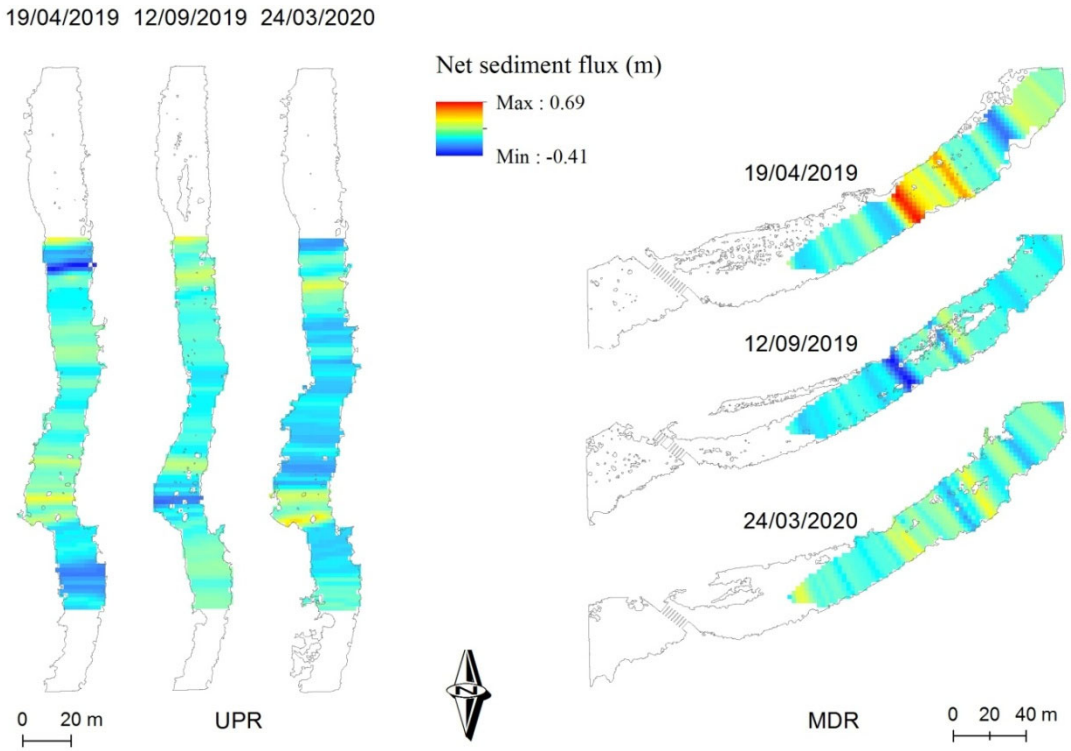

Figure 6. Normalized net sediment flux for each budget cell in the three peak flows analyzed along the two reference channel reaches (RCR).

4.2. Changes in the bed elevation profiles determined using VHR DTM

Variations in the longitudinal and cross-sectional bed elevation profiles make up an indicator of changes in flow velocity and competence, which condition erosion and deposition. Considering the LiDAR-derived bed elevation change along the channel centerline between 2018 and 2020, a substantial variation was observed along both RCRs during the survey periods (Fig. 7). From November 2018 to September 2019 net deposition predominated, increasing the bed height by between +0.12 and + 0.33 m, especially in the middle RCR. In the following period (September 2019 to January 2020) the pattern of change differed between the two channel stretches, erosion dominating in the upper RCR and the spatial variability of sediment budgets in the middle RCR. In the latter, the sub-bankfull discharge of 12 September, 2019 caused scouring upstream and vertical accretion downstream, without affecting the raised zone of an intermediate high bar, which remained

almost completely submerged. Finally, the longitudinal profile of July 2020, due mainly to the bankfull peak flow of 24 March 2020, reflected a general lowering, so that the initial bed surface profile was largely recovered. These changes suggest that, overall, there was more bed aggradation during the flash flood event and more erosion when the events of moderate magnitude occurred. For the analysis period a quasi-equilibrium is observed for the bed profile in the more entrenched upper RCR, since the mean elevation of the active bed did not experience significant temporal variations.

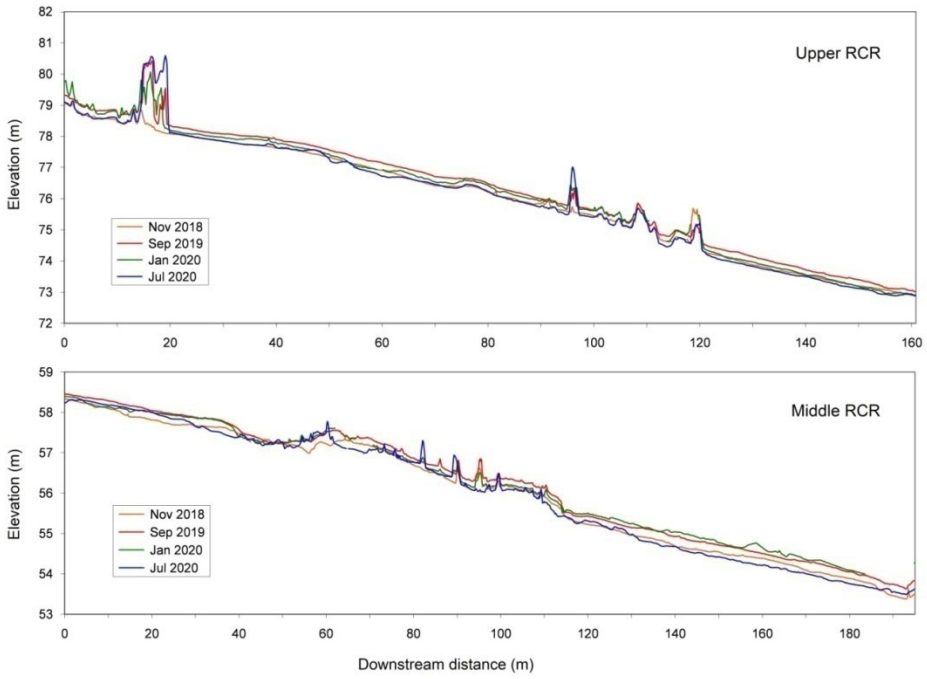

Figure 7. Longitudinal bed elevation profiles extracted from TLS datasets for each monitoring survey and RCR.

The shapes of the initial (2018) and final (2020) thalweg profiles are relatively similar here, except in certain locations of bedforms: the formation of a new longitudinal bar and the destruction of another, pre-existing one led to a bed raising and lowering, respectively. In contrast, the middle RCR underwent a relatively greater variation in bed elevation as a result of spatial differences in grain size and its pre-existing topography, conditioned by a high and stable central bar that acted as an obstacle to the flow at high water stages. Similar effects have been described by other authors for this type of channel, during recent monitoring periods (Norman et al., 2017). The rectilinear form of both series of profiles is interrupted only by local ruptures associated with transverse bars that produce short-distance variations in the stream power. Similar to the findings of Pitlick and Cress(2002),

these are not strongly influenced by transitions in reach type (alluvial to quasi-alluvial) or by junctions with tributaries.

The spatial variation downstream of the differences in transverse changes in bed elevation for each event and section is depicted in Figures 8 and 9. Specifically, the scatter plots in Figure 8 show the spatial patterns of the relationships between the changes in the bed height of the center line (CL) and the changes to the left along lateral lines 3 m (CLL) and 6 m (LL) from the CL and to the right, also at 3 m (CLR) and at 6 m (RL). Ten patterns of lateral net sediment fluxes were found, with a marked differentiation between the upper and middle reaches. During the April 2019 event, with respect to the CL, in the upper RCR, the erosion rates and deposition were similar on the left and the deposition decreased towards the right bank. In this stretch an equilibrium between erosion and deposition in the CL seemed to break slightly in favor of erosion, which was more prevalent on both lateral bed sides. By contrast, the morphological adjustments in the middle RCR showed more marked differences between the CL and the lateral bed extremes. In the major flood, aggradation processes were dominant in the entire transversal bed, being more evident towards the banks than in the center of the channel. At sub-bankfull discharge, the balance between erosion and deposition close to the CL gave way to a relative increase in sedimentation in the lateral zones, while under bankfull conditions, represented by the March 2020 event, deposition predominated in the CL and downcutting in the LL.

The profiles in Figure 9 display the difference in behavior between the CL and the lateral bed zones for each peak flow, according to the distance downstream. This was defined by calculating the differences in bed height (Δe)of RL and LL relative to the Δe CL.

For the larger flood event, the difference profile of the CL showed greater similarity to that of the right part than to that of the left, although downstream the Δe RL values tended to homogenize with those of the rest of the bed within a general process of bed aggradation. In the middle RCR the values of Δe LL (0.25 to 0.40 m), higher than the positive differences of Δe CL (ranging from 0 to 0.22 m), suggest erosion rates for this event on the left lateral bed ranging from 0.18 to 0.25 m, coinciding with the greatest deposition in a transverse medial bar. The rest of the section registered more deposition in the lateral zones than in the central zone, as can be inferred from the position of the LL and RL difference profiles below CL when they adopt negative values. The September 2019 event involved a more uniform bed downgrading in the upper RCR than in the middle RCR. Along the upper reach, the LC change profile remained almost entirely below 0 m with Δe values generally lower than those of LL and RL, which denotes greater erosion in the areas

closest to the banks. Downstream, in the middle RCR the left margin had a geomorphic activity similar to that of the central part, while the area near the right margin acted alternately as a site of scour and vertical accretion.

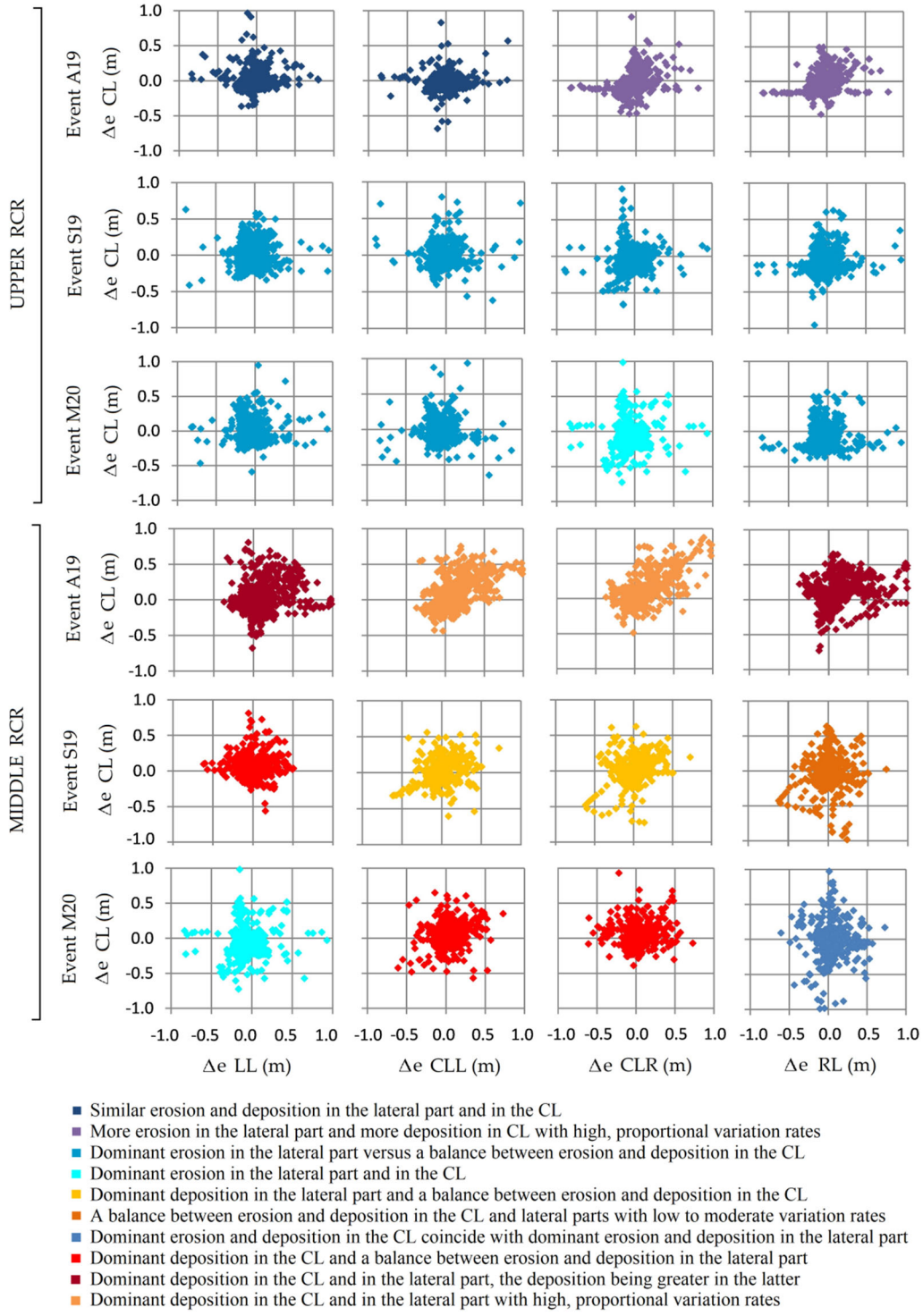

Figure 8. Relationships between Δe CL and bed elevation differences in lateral channel lines with a separation distance of 3 and 6 m on the right (Δe CLR; Δe RL) and left (Δe CLL; Δe LL) sides. Events of 19-20 April, 2019, 12 September, 2019, and 24 March, 2020.

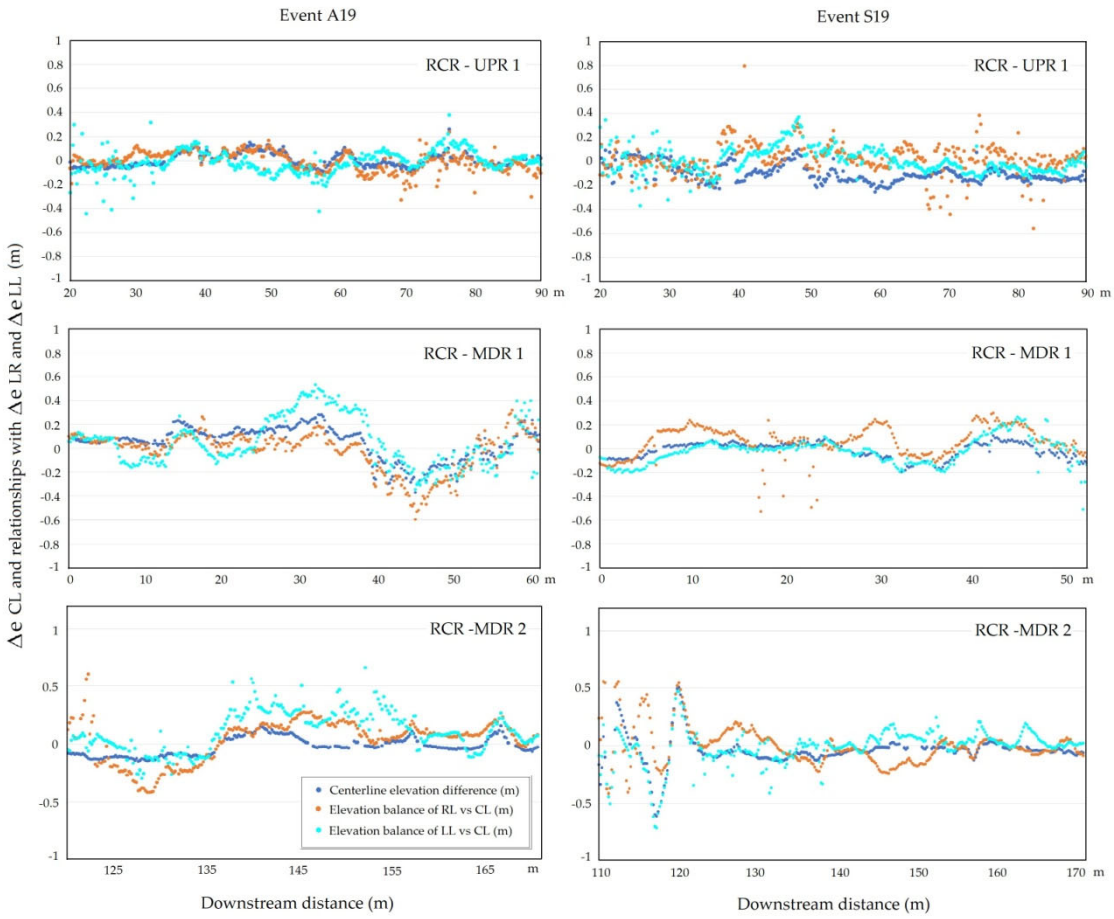

Figure 9. Scatter plots comparing the differences in Δe RL and Δe LL with respect to Δe CL, versus the downstream distance in the upper and middle RCRs (UPR and MDR respectively). Peak flow events of 19-20 April, 2019 (Event A19) on the left and 12 September, 2019 (Event S19) on the right.

There was a noticeable dispersion in the bed elevation balances at the beginning of RCR-MDR 2; this may represent interpolation errors caused by low TLS point density and inconsistent spatial geometry between the surveys in this portion of the survey area.

The longitudinal and cross-sectional channel profiles got for the PBSAs (Figure 17) show, in great detail, the changes produced at the geoform level. The A'-A to F-F' profiles show the partial disaggregation of a longitudinal central bar and the lowering of the main active channel during the analysis period in the upper RCR.

It is worth noting the contrast between the uniform lowering that the profile of July 2020 exhibits with respect to the initial profile at the head of the bar (D-D') and the inversion of the zones of bed accretion and scour downstream (F-F'). Field surveys confirmed that the

central part of the bar (2-4 m in E-E'), composed of the coarsest material (gravel and pebbles) and with an imbricated and massive structure, was the most stable site.

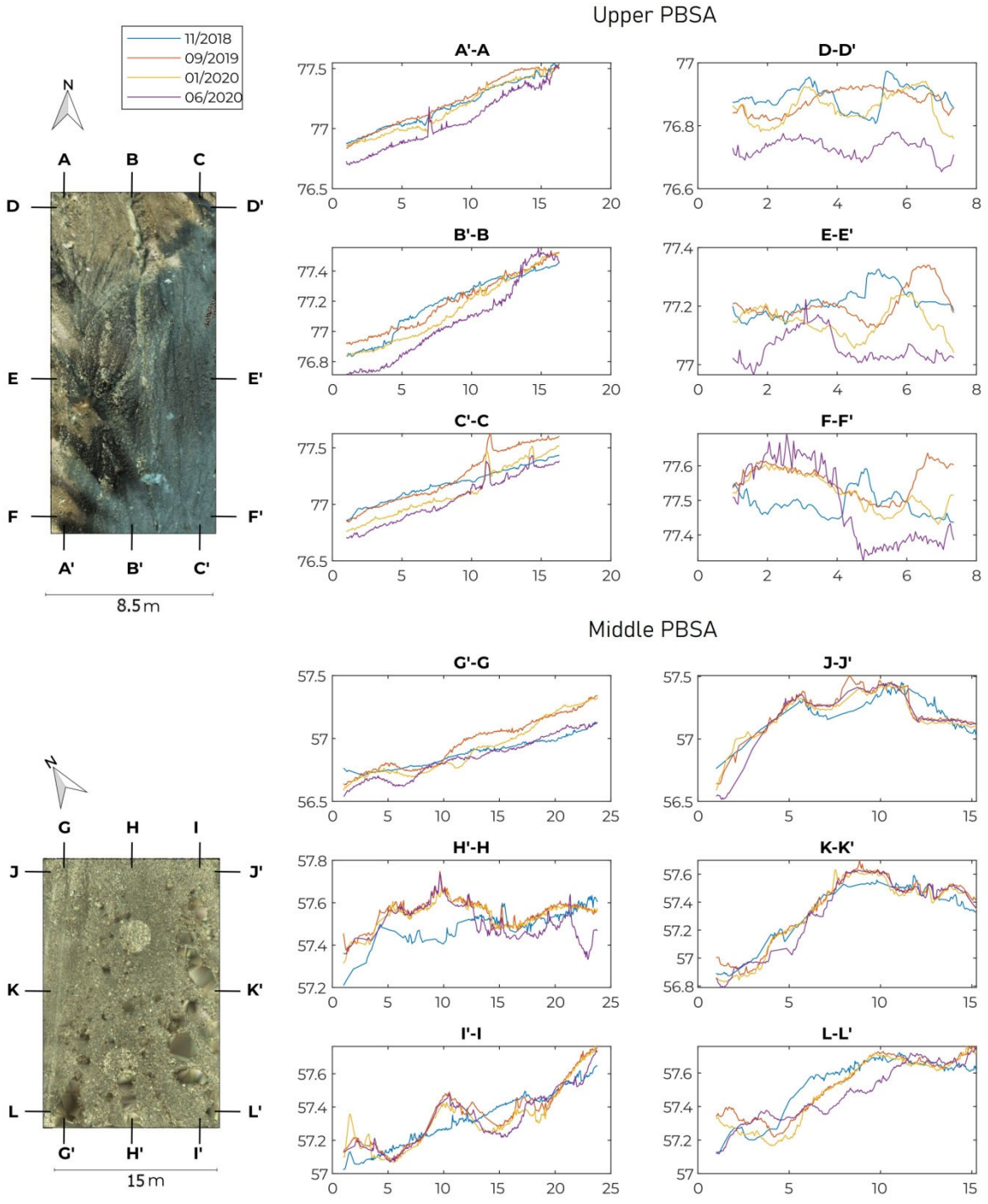

Figure 10. Longitudinal and cross-sectional channel profiles, extracted from TLS datasets, for each peak flow and monitoring bed survey area (upper and middle PBSAs).

The PBSA in the middle reach encompasses the transition zone to the medial bar head, with crude horizontal bedding and small-scale gravel cross-strata. As the RCR-scale longitudinal profiles have already reflected, the bed surface along the talweg rose during April 2019, fell slightly in September 2019, and recovered its initial profile after the March 2020 bank flow (G'-G). Considering the entire period, a slight net deposition of 0.1 to 0.2 m (J-J') (K-K') in the zone of entry to the bar platform and a decrease of 0.05 to 0.23 m (L-L') in the bar supra-platform deposits were observed.

4.4. Stream power maps and relationships

Hydraulic variables related to stream power (including υ, τ_0, τ_c, ω, $\partial\omega/\partial s$, and ε) were estimated continuously along each study RCR for the three main peak flows. Table 5 shows some statistical descriptors for them and Fig. 11 displays the grids of the ω and ε (ω-ω_c). The resultant maps allowed us to infer variations in their values that were then related to the spatial patterns of sediment budgets in order to explain better the processes that control the morphological channel adjustments. The flow velocity ranged from 1.10 m s^{-1}, in sections with greater roughness, dominated by pools, blocks, and scrubs, to 2.65 m s^{-1}, at riffle sites. Specifically, the greatest increases in flow velocity occurred in the steepest and narrowest stretches composed of cohesive materials. This is consistent with the view that an entrenched channel tends to remain narrower in bedrock than in gravel bed at similar flow stages (Finnegan et al., 2005).

A more effective indicator for the calculation of the sediment carrying capacity is the relationship between the boundary shear stress (τ_0) and the critical shear stress (τ_c). The spatial variability of both parameters was highly significant in the analyzed reaches, where alternating changes in the bed roughness caused appreciable turbulence and velocity fluctuations. Heterogeneities due to variations in grain sizes and bedforms may create substantial velocity and shear stress variations across the channel or downstream during a single discharge (Wohl, 2000). Consequently, the maps exhibit, in both reaches, a wide patchwork of τ_0 values, ranging from 1.2 to 160 N m^{-2}, and somewhat less variability in τ_c (23.1 to 79 N m^{-2}). These ranges were practically maintained downstream, although the variability among sections regarding shear stress was lower in MDR than in UPR. The τ_0/τ_c ratio also varied from one stretch to another, so that its average value was considerably higher in the upper reach (2.4), compared to that in MDR (1.6). In accordance with this, the shear stress was more than double the critical shear stress in UPR, which implies a high

bed-load capacity and channel degradation. Downstream, incision in the middle reach was likely, but morphological adjustments associated with high rates of sediment entrainment and mobility remained.

Table 5. Statistical descriptors for hydraulic variables related to stream power during the peak flows of 19 April, 2019 (A19), 12 September, 2019 (S19), and 24 March, 2020 (M20) in the upper and middle RCRs. The values are extracted from the set of cells (i) in each RCR.

	SV	υ			τ_0			ω			δω/δs			ε		
		A19	S19	M20	A19	S19	M20	A19	S19	M20	A19	S19	M20	A19	S19	M20
Upper RCR	mean	2.16	1.66	1.83	96.5	70.2	78.4	212.9	119.1	146.2	-0.6	-0.1	-0.5	157.3	59.6	85.1
	min	1.34	1.12	1.10	34.2	28.1	31.8	46.5	32.2	35.4	-14.5	-8.3	-10.7	-72.9	-89.2	-119.5
	max	2.65	2.10	2.30	160.3	103.8	118.8	371.4	209.5	245.2	14.9	10.6	5.8	333.4	166.1	189.2
	error	0.03	0.02	0.02	2.21	1.44	1.66	6.25	3.29	3.93	0.80	0.55	0.35	7.69	4.42	5.00
	σ	0.29	0.21	0.23	24.7	16.1	18.6	69.9	36.8	43.9	6.3	4.3	3.3	86.0	49.4	55.9
	K	0.53	-0.11	0.72	-0.12	-0.21	0.00	-0.37	-0.36	-0.03	1.01	1.26	0.06	0.29	0.15	1.11
	Sk	-0.73	-0.54	-0.80	0.43	-0.48	-0.53	-0.44	-0.34	-0.58	0.58	0.57	0.56	-0.84	-0.68	-1.03
Middle RCR	mean	1.95	1.50	1.55	84.7	59.8	69.9	170.8	93.8	113.6	-0.6	-0.4	0.0	102.8	22.6	31.0
	min	0.50	0.37	0.28	1.2	0.73	0.39	0.59	0.27	0.11	-14.1	-6.2	-8.0	-98.8	-176.5	-136.2
	max	2.38	1.95	2.05	146.1	110.6	125.6	344.3	215.9	253.9	15.8	6.8	7.2	306.6	149.3	167.9
	error	0.03	0.03	0.03	2.55	1.89	2.20	6.56	3.98	4.88	0.73	0.37	0.31	9.49	6.00	6.19
	σ	0.29	0.25	0.28	25.2	18.6	21.7	64.7	39.2	48.0	6.0	3.0	2.7	92.5	58.5	60.4
	K	8.56	6.50	5.73	1.55	1.63	1.26	0.53	0.93	0.28	0.37	-0.08	0.50	0.47	0.93	0.16
	Sk	-2.12	-1.69	-1.37	-0.32	0.03	-0.26	0.26	0.67	0.47	0.57	0.57	0.56	0.42	-0.45	0.07

υ = flow velocity (m s^{-1}); τ_0 = shear stress (N m^{-2}); ω = mean stream power (W m^{-2}/m); δω/δs = mean stream power gradient (W m^{-2}/m);ε = excess energy (W m^{-2}/m).

Since ω(i) results from the multiplication of υ by τ_0 for a given cell i, the spatial pattern of ω shows a large variability, because of fluctuations of both variables. Particularly, the ω values had an excellent power function fit with υ and τ_0 (r^2 = 0.91 and 0.98, respectively). The mean stream power also showed an excellent fit with the Froude number (r^2 = 0.84) and the energy slope (r^2 = 0.87) when using the same function type, but its relationship with the hydraulic radius was worse (r^2 = 0.45 for a polynomial regression).

In the RCRs studied, the mean stream power during the peak flow of 19-20 April 2019 varied from 0.6 to 371.4 W m^{-2}, the excess energy from 333.4 to -98.8 W m^{-2} (Table 5, Fig. 11), and the stream power gradient from -14.5 to 15.8Wm^{-2}/m (Fig. 12) (the upper limits of color displayed in Figs. 11 and 12 for such variables encompass 95% of the data). Note, however, that over 75% of the $\partial\omega/\partial s$ values fell within the range 6 to -6 Wm^{-2}/m and that the extreme data reflect local abrupt changes in ω.

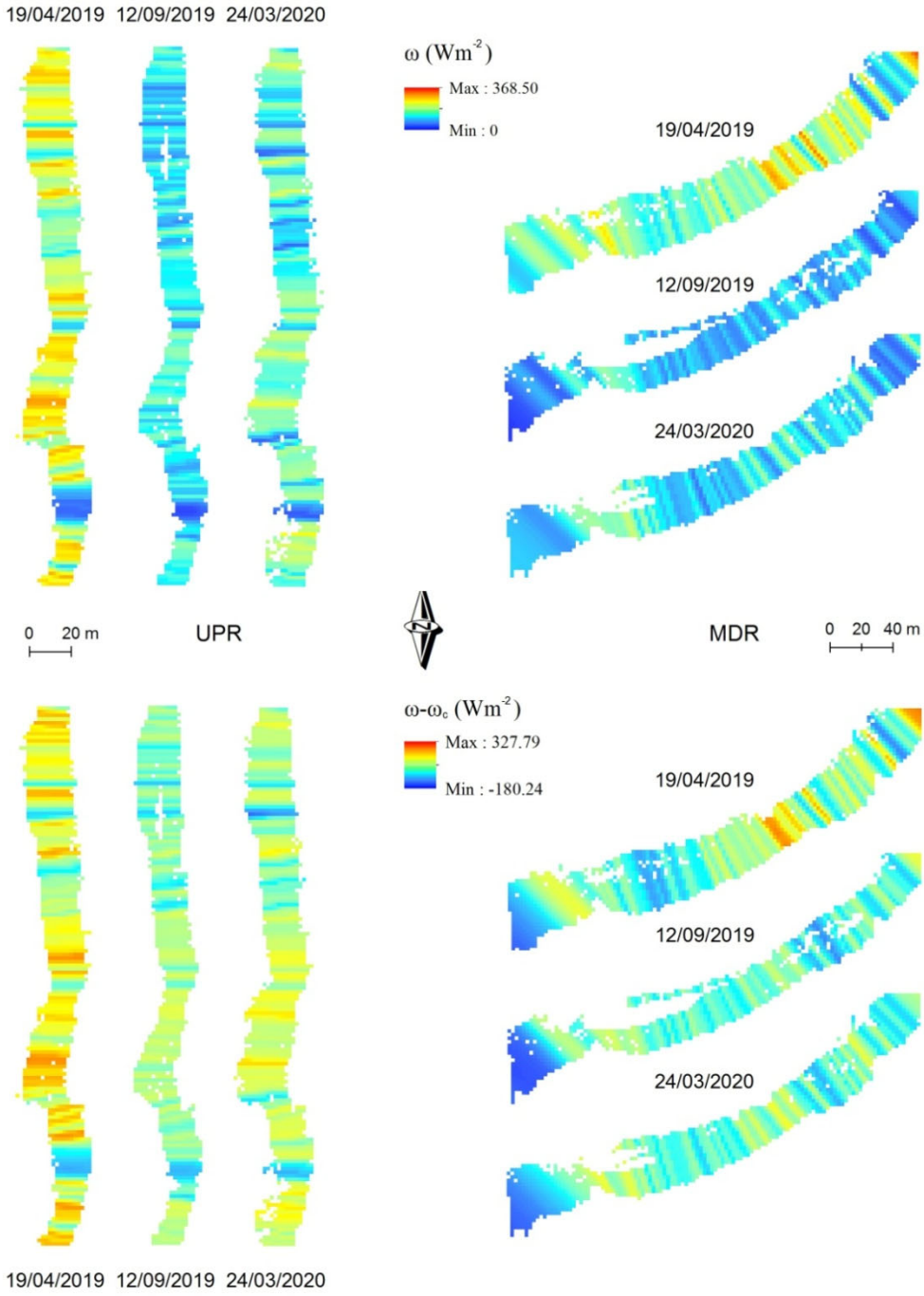

Figure 11. Values ofω, ∂ω/∂s, and ω/ωc calculated by cell using spatial interpolation of Hec-RAS data at equidistant (2.0-3.5 m) cross-sections, estimated for the three peak flows in the upper and middle RCRs (UPR and MDR respectively). The maximum color limits encompass 95% of the datasets.

As for the flow velocity and the shear stress, the highest values of mean stream power were concentrated in entrenched channel cross-sections, along straight to sinuous stretches, and locally over steep riffles characterized by high near-bed velocity gradients. This pattern is linked to incision processes in several Mediterranean ephemeral streams (e.g., Garzón and

Alonso, 2002, Hooke, 2006,Ortega et al., 2014). However, we observed a significantly unconventional behavior in the gravel beds studied here, where an important transitory erosion was often followed by extraordinary mobility of the bed materials, which caused channel aggradation in the more important events.

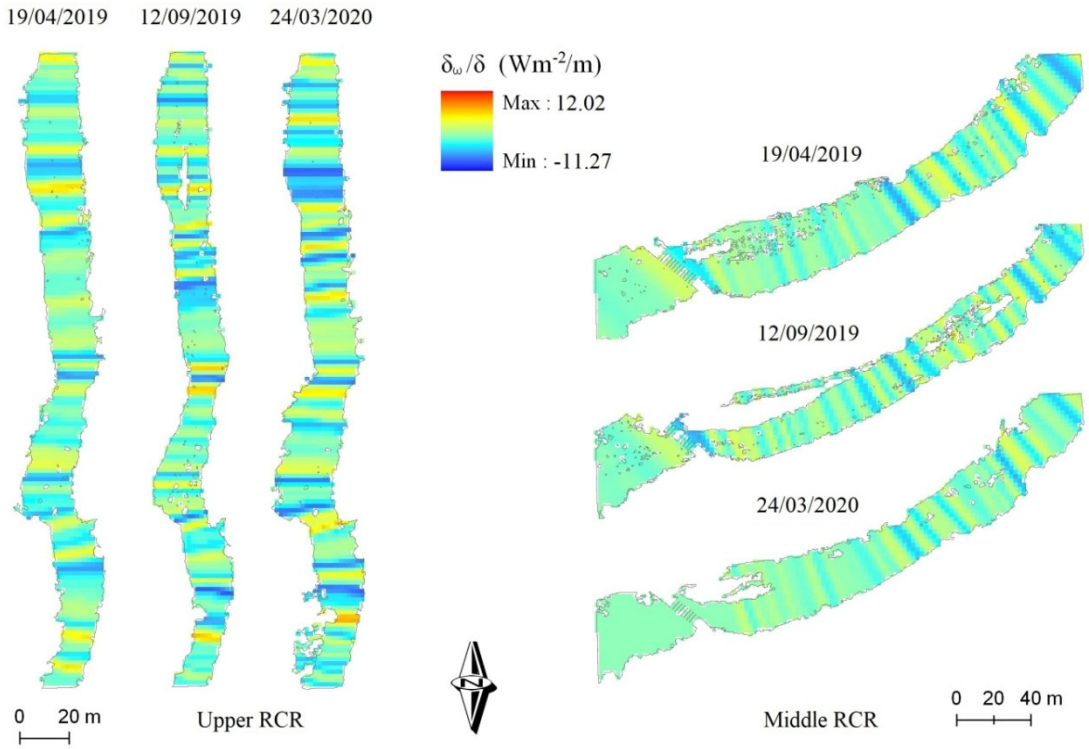

Figure 12. Values of $\partial\omega/\partial s$ calculated by cell using spatial interpolation of Hec-RAS data related to equidistant (2.0-3.5 m) cross-sections in the upper and middle RCRs, for the peak flood of 19-20 April 2019. The maximum color limits represent 95% of the datasets.

The distribution of the ω/ω_c ratios was also skewed for both RCRs and the distinct flood events, with maximum values very distant from the mean and median. In the April and September events maximum ratios around 10 and 7, respectively, were reached in the two reference stretches, with much lower and different medians depending on the reach. Specifically, during the peak flood of 19-20 April 2019, the ω/ω_c median was 2.7 in UPR and 1.2 in MDR.

Furthermore, we have verified that the pattern described by other authors for gravel-bed ephemeral streams with a more heterogeneous channel geometry and planform is not fully reproduced here. Conesa-García et al. (2020b) found higher energy balance values in less entrenched and less incised cross-sections transitioning to channel widening. By contrast, along the straight and slightly sinuous stretches analyzed here the most significant energy

balances occurred locally in the more entrenched sections with a low to moderate width-to-depth ratio and high transport capacity. It should be considered that in such gravel-bed streams the grain roughness may become more influential than the changes in bed slope with regard to variations in ω_c (Rickenman, 2011; Camenen et al., 2012; Conesa-García et al., 2020b).

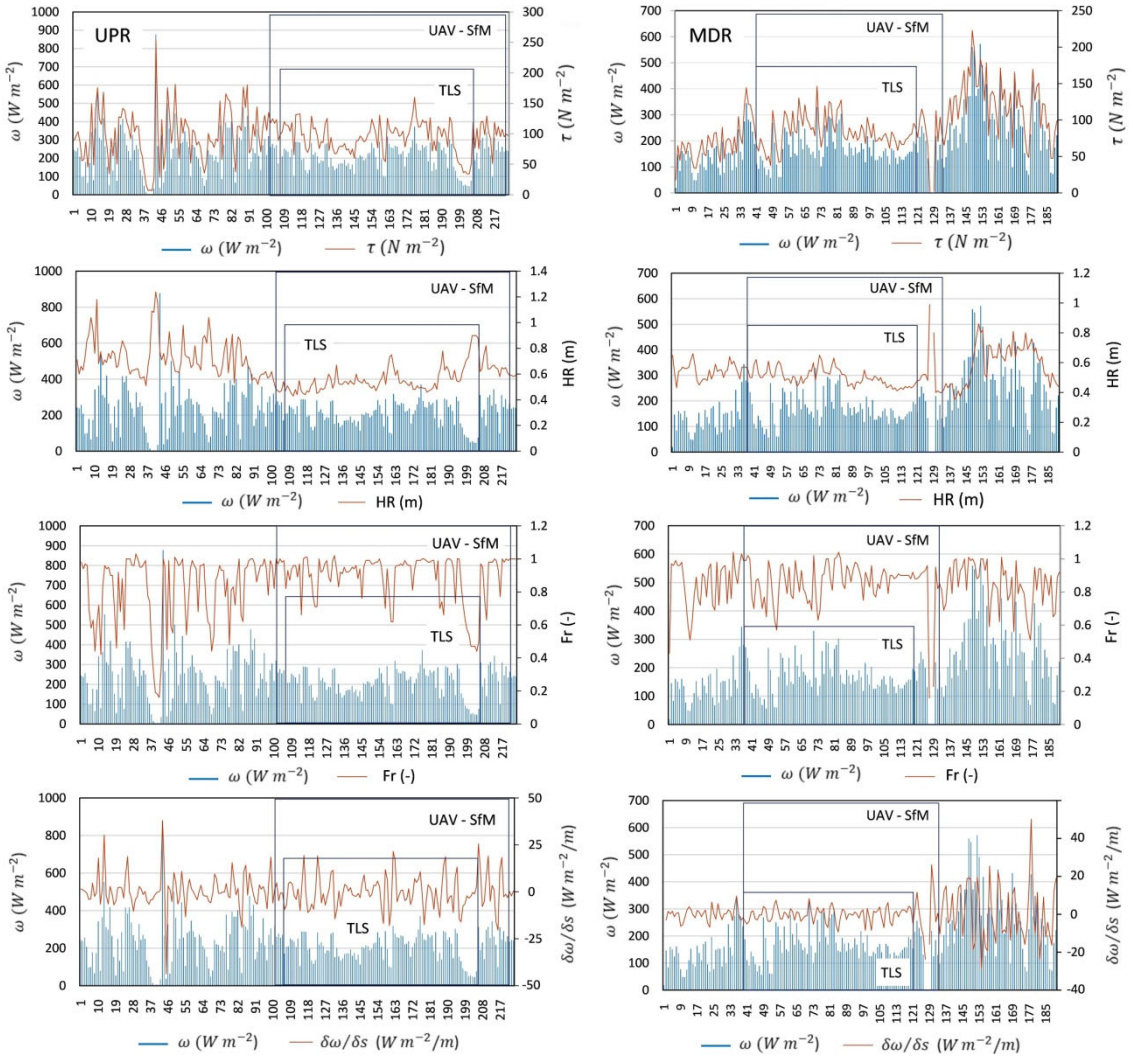

Figure 13. Spatial variability in the relationships of ω with τ_0, R, Fr, and $\partial\omega/\partial s$ along the UPR (223 equidistant cross-sections, 2.0-3.5 m apart) and the MDR (191 cross-sections), including their respective RCR covered by UAV-SfM and TLS. Peak flood of 19-20 April 2019.

The spatial variability of ω was contrasted with that of other significant hydraulic variables (τ_0, R, Fr, and $\partial\omega/\partial s$) in a downstream direction along the entirety of the stretches under analysis. Figure 13 depicts these comparisons for the flood of April 2019, considering all

the cross-sections included in the complete stream reaches and the RCRs. As described above, variations of ω in both RCRs closely followed the pattern of variability observed in the shear stress and Fr distributions. The only nuance was found in the frequency with which Fr reached the value 1 in both stretches, depending on the mean stream power registered. The ω *versus* Fr relationship enabled us to establish, in our case, the value 200 W m^{-2} as the threshold above which the limit defining the subcritical regime is exceeded. This condition occurred in more than 50% of the cross-sections along the UPR, but it was barely reached in the MDR. On the other hand, ω maintained a poorer spatial relationship with the hydraulic radius (R), which was often due to a greater influence of the slope and bed roughness on the stream power. This was particularly evident in the UPR, outside and within the RCR monitored using UAV-SfM and TLS, where increases in ω coincided with decreases in R, and *vice versa*.

The relationship between ω and $\partial\omega/\partial s$ revealed downstream changes in the energy gradient as a function of the mean stream power generated in each budget cell. In the case of the April 2019 event, the highest values of $\partial\omega/\partial s$ were often preceded by high values of ω (above 300 W m^{-2}), while the $\partial\omega/\partial s$ close to zero or with a negative sign occurred along sections with low-to-moderate mean stream power ($\omega <$ 200 W m^{-2}). Except for the final part of the middle reach, where road-crossing drainage culverts locally disturbed the flow, the fluctuations in $\partial\omega/\partial s$ were less pronounced and lower in the MDR than in the UPR.

4.3. Stream power variations versus changes in bed stability

Transport and high incision efficiency often occur when the limiting shear stress and stream power exceed the resistance of the bed materials to be mobilized (Lague, 2014). The bed stability indices used here follow this criterion, but in armored bed channels such as ours the heterogeneity of mixed-grain-size material- including sand, gravel, and pebbles- implies non-unimodal distributions that have an important influence on the initial bedload motion and complicate the bedload transport-rate estimations (Almedeij, 2002).In addition, transport-capacity-based assessments in this type of gravel-bed stream produce results that are sometimes not very consistent with the observed net sediment fluxes, due to discrepancies attributed to non-uniform grain sizes, bed surface armoring, and bedform variability (Buffington and Montgomery, 1997;Hassan et al., 2008; Lisle and Church, 2002).

In the RCRs of this study, high bed armoring and a coarsening-upward trend in most bed deposits led to a relationship between the stability of the armored surface layer and sub-surface detrital layer with the topographic changes observed using VHR DTM. Specifically, relationships between the RBS index attributable to each of these layers and the differences in net bed elevation provided by these spatial models (Δe (SfM-TLS)) after the April flood event were obtained, with the following results:

$$\Delta e\ (SfM\text{-}TLS) = 0.167 ln(RBSsup) + 0.409 \qquad R^2 = 0.715 \qquad (7)$$

$$\Delta e\ (MfS\text{-}TLS) = 0.122 ln(RBSsub) + 0.506 \qquad R^2 = 0.637 \qquad (8)$$

Using regression equations with a logarithmic function, the best fit was achieved for the materials that make up the surface armored layer. This conclusion together with the recommendation to use D_{84} for the bed stability calculations in these cases (Martín-Vide, 2007) led to the adoption of both criteria to estimate RBS. By comparing the map of stream power (Fig. 7) with the spatial distribution of bedforms and bed stability indices, we explored whether the stream power thresholds set by other authors (e.g. Magilligan, 1992; Stacey and Rutherfurd, 2007) to evaluate transport efficiency classes in non-ephemeral, gravel-bed streams are valid for this GBES type. Concerning the stream power thresholds, these authors proposed 35 Wm^{-2} for riverbed erosion and 300 Wm^{-2} for overall morphological channel changes. In our case, and as already evidenced by Conesa-García et al. (2020b) in the upper Mula stream, a high spatial heterogeneity of bed forms and sediment grain sizes was observed, leading to stability changes over relatively short distances, which locally affected the stream power required for sediment entrainment. The threshold of 35 Wm^{-2} did not coincide with that of bed instability in many of the cross-sections studied here (Fig. 14), and in other cases it did not coincide with the removal threshold, established from negative values of Δe when TLS was used. The ω thresholds to initiate particle movement in unstable bed sections (RBS<1) ranged between 35 and 43.7 Wm^{-2} for the minor peak flow. In the April flood event these thresholds were exceeded in almost all cases because of the greater flow energy generated. In addition, a minimum of 46.5 Wm^{-2}in the upper RCR and of 66.4 Wm^{-2} in the middle RCR was required to cause bed incision along the stretches monitored by TLS. Both events exhibited a very efficient

transport capacity, with τ exceeding τ_c in more than 95% and 86% of the cross-sections in the upper and middle reaches, respectively (Table 6).

Figure 14. Mean stream power (ω) versus the Relative Bed Stability (RBS) and Bed Form Stability (BFS) indices estimated in cross-sections along the upper and middle RCRs, in a downstream direction. Flow peaks of 19-20 April 2019 (a) and 12-13 September 2019 (b).

Although the results found for RBS>1cannot be considered statistically significant, the difference in the mean ω between the stable and unstable RCR beds was quite relevant, with the event magnitude being as influential on the sediment transport as the bed grain size. This contrast was somewhat similar in both stretches, which contradicts a progressive decrease in downstream flow competence. The ω needed for transport to start varied only slightly from section to section, so, according to the relationships between the driving forces and sediment loading, particle size and bedforms became two crucial factors in the assessment of morphological bed alterations.

Table 6. Statistical descriptors got for ω from different ranges of bed stability indices (RBS and BFS), using the stream power thresholds proposed by Magilligan (1992) and Stacey and Rutherfurd (2007) for the evaluation of flow competence in relation to morphological change in perennial, gravel-bed streams.

		Peak flow of 19-20 April 2019								Peak flow of 12-13 September 2019							
	RG	ω for RBS < 1				ω for RBS > 1				ω for RBS < 1				ω for RBS>1			
	I(ω)	<35	35-150	150-300	>300	<35	35-150	150-300	>300	<35	35-150	150-300	>300	<35	35-150	150-300	>300
Upper RCR	Ncs	0	22	90	9	0	4	0	0	1	89	29	0.0	1	5	0	0
	% T	0.0	17.6	72.0	7.2	0.0	3.2	0.0	0.0	0.8	71.2	23.2	0.0	0.8	4.0	0.0	0.0
	% Ac		96.8				3.2				95.2				4.8		
	% I(ω)	-	18.2	74.4	7.4	-	100	-	-	0.8	74.8	24.4	-	6.7	83.3	-	-
	Min	-	74.3	152.4	302.8	-	47.7	-	-	34.8.	51.2	150.3	-	32.2.	36.1	-	-
	Med	-	123.7	230.9	321.8	-	49.8	-	-	34.8	110.3	164.2	-	32.2	47.7	-	-
	Max	-	270.9	299.0	371.4	-	54.8	-	-	34.8	144.5	209.5	-	32.2	61.7	-	-
	σ	-	41.2	41.5	22.1	-	3.6	-	-	0.0	25.4	13.3	-	0.0	10.1	-	-
	RG	ω for RBS < 1				ω for RBS > 1				ω for RBS < 1				ω for 1 > RBS			
	I(ω)	<35	35-150	150-300	>300	<35	35-150	150-300	>300	<35	35-150	150-300	>300	<35	35-150	150-300	>300
Middle RCR	Ncs	3	29	54	3	0	9	0	0	3	74	8	0	0	13	0	0
	% T	3.1	29.6	55.0	3.1	0.0	9.2	0.0	0.0	3.1	75.5	8.1	0.0	0.0	13.3	0.0	0.0
	% Ac		90.8				9.2				86.7				13.3		
	% I(ω)	3.6	34.1	63.6	3.6	-	100	-	-	3.5	87.1	9.4	-	-	100	-	-
	Min	0.6	91.8	151.2	303.1	-	57.1	-	-	0.2	43.7	150.1	-	-	36.8	-	-
	Med	0.9	130.2	203.4	325.8	-	92.2	-	-	0.3	93.4	177.9	-	-	58.8	-	-
	Max	1.2	149.6	293.4	344.3	-	128.1	-	-	0.3	149.7	215.9	-	-	86.1	-	-
	σ	0.4	16.0	42.3	21.0	-	30.9	-	-	0.0	26.3	24.19	-	-	17.0	-	-

I(IR) = IR interval; RG = RBS range for which ω (mean stream power) values are calculated; I(ω) = ω interval; Ncs = Number of cross-sections with ω value included in each I(ω); % T = percentage of the number of cases in each ω interval regarding the total number of cases in the entire channel reach; % Ac = accumulative percentage of %T; % I(ω)= percentage of cases in each ω interval regarding the total number of cases in each RBS range. Min, Med, and σ = minimum, median, and standard deviation values of ω for each I(ω) within each RBS range.

The interval of ω commonly associated with moderate to significant morphological changes in non-ephemeral gravel-bed streams (35-300 W m^{-2}) showed different patterns here in terms of magnitude and frequency. The unstable bed sections supported a substantially higher average energy in the upper RCR than in the middle RCR. In particular, most of the ω values along the upper RCR (72nd percentile) on 19-20 April 2019 were in the 150-300 Wm^{-2} interval, scoring a mean of 211.2 Wm^{-2}, while in the middle RCR the 72nd percentile dropped to 45% and the mean to160.5 Wm^{-2}. For a peak discharge of 21.9 m^3/s, the upper reach stream showed a higher transport capacity than the middle stretch (31.3 m^3/s) to trigger bed degradation processes (e.g. bed scouring and downcutting). Active bed forms predominated upstream, while erosion-resistant bed forms and aggradation gravel layers had a greater presence downstream in the middle stream reach.

This is reflected in the third quartile of the BFS values (Q3 between 0.2 and 0.4 in the upper RCR and between 0.4 and 0.6 in the middle RCR, considering the wetted perimeter during the largest runoff) (Fig. 14). Regarding the frequency of the ω values within this range, the percentage was slightly higher (89.6%) in the upstream reach than downstream (84.6%). However, ω values above a new sub-threshold around 150 Wm^{-2} were found to cause high mobilization of surface gravels and active alluvial bars. The most entrenched and steepest stretches involved a higher percentage of cases above this limit than those with less embedding and bed slope. In fact, the % ω for the 150-300 Wm^{-2} interval increased from 17.6% in the upper RCR to 29.6% downstream (Table 6). By contrast, values from 35 to 150 Wm^{-2} were associated with the removal of bank-failure deposits and moderate changes in active low bars. The greatest morphological adjustments, related to ω values above 300 Wm^{-2}, were more frequent along the upper channel reach, where phenomena of lateral erosion and intense reactivation of high, scarcely-vegetated bars occurred. In all of these situations, gravel-bed armoring was reinforced by new inputs of coarse sediments. With the lower peak flows, such as the September 12-13, 2019 event, selective transport dominated, as gravel and sand were mobilized, but not pebbles.

Table 7. Regression equations defining the relationships of Δe with ∂ω/∂s, ε, and Relative Bed Stability (RBS) at the scale of cell i in the flash flood of April 2019. Datasets of SfM-MVS and TLS extracted for the upper (UPR) and middle (MDR) reaches. Significance level (p-value) < 0.05.

RCR	Δe vs HV	Method	Num. cells	Equation	r^2
UPR	Δe vs ∂ω/∂s	SfM	73	---	0.001
		TLS	73	---	0.000
MD	Δe vs ∂ω/∂s	SfM	72	---	0.020
		TLS	72	---	0.003
UPR	Δe vs ε	SfM	50	Δe (SfM) = 0.0004 ε + 0.179	0.597
		TLS	42	Δe (TLS) = 0.0005 ε - 0.097	0.453
MDR	Δe vs ε	SfM	38	Δe (SfM) = -0.0002 ε + 0.221	0.564
		TLS	46	Δe (TLS) = -0.001 ε + 0.053	0.521
UPR	Δe vs RBS	SfM	50	Δe (SfM) = -0.135 RBS + 0.296	0.639
		TLS	42	Δe (TLS) = -0.218 RBS + 0.078	0.606
MDR	Δe vs RBS	SfM	44	Δe (SfM) = 0.137 8RBS + 0.132	0.648
		TLS	40	Δe (TLS)= 0.321 RBS - 0.198	0.520

Table 7 lists the relationships of Δe with ∂ω/∂s, ε, and RBS in the flash flood of April 2019, based on SfM-MVS and TLS datasets. A relatively close relationship of Δe with

excess energy and bed stability was achieved usingSfM data, which provided the best fit (r^2 of 0.56 to 0.60 for Δe versus ε, and around 0.65 for Δe versus RBS). However, the TLS technique gave good results, with some statistical significance, only when associating Δe with RBS, mainly along the upper reach ($r^2 = 0.61$, p-value <0.05). The higher correlation established with RBS reflects the strong influence that flow competence exerted, through the selective transport of inhomogeneous granular material (such as sand, gravel, and pebbles), on the bed stability. The excess energy expenditure implies a more moderate fit with the morphological variations at the cell level, a better result being foreseeable when a certain consecutive number of budget cells are considered downstream.

4.4. Sediment budgets and fluxes versus stream power

The point clouds in Figure 15 show the D and E values for the peak flows of April 2019, September 2019, and March 2020 for each cell i, in relation to the mean stream power gradient ($\partial\omega/\partial s$). Positive and negative values depict surface lowering and raising, respectively. *In situ* field observations made after these events corroborated the morphological adjustments in both directions, with the concurrent deposition and erosion on a metric and centimeter scale. Assuming $\partial\omega/\partial s$ in a given cell leads to the strongest expression of sediment change in the nearest cell downstream from it, scatter plots relating $\partial\omega/\partial s(i)$ to $\Delta V(i+1$ to $i+3)$ were also used to explain the influence of the energy gradient on the net flux variations immediately downstream (Fig. 16). In all cases, the effect of the four hypothesized geomorphic trends described in Table 1 was discriminated at the cell scale.

Several patterns of variation were found in this type of relationship, depending on the section in question, the predominant geomorphic process, and the event magnitude: 1) For the three events, regardless of the peak flow reached, the pattern differed greatly between the two stretches, in relation to the premises established for the balance $\omega - \omega_c$ in each pair of neighboring cells. Among the upper RCR relationships practically only cases 1 and 3 were present, while in the middle RCR all cases were represented. 2) During the event of greatest magnitude, the upper section experienced greater net erosion than the middle section, especially in the cells, where ω increased downstream and exceeded ω_c for both budget cells (case 1), coinciding with $\partial\omega/\partial s$ values having a positive sign. Also, there were quite a few cross-sections with excess energy despite a decrease in ω downstream (case 3), resulting in minor deposition that was unable to compensate for transitory erosion. A

similar response was found by Conesa-García and García-Lorenzo (2009) in EGBSs draining metamorphic terrains. Consequently, during this type of event the upper reach acts as an important source of sediment for downstream reaches.

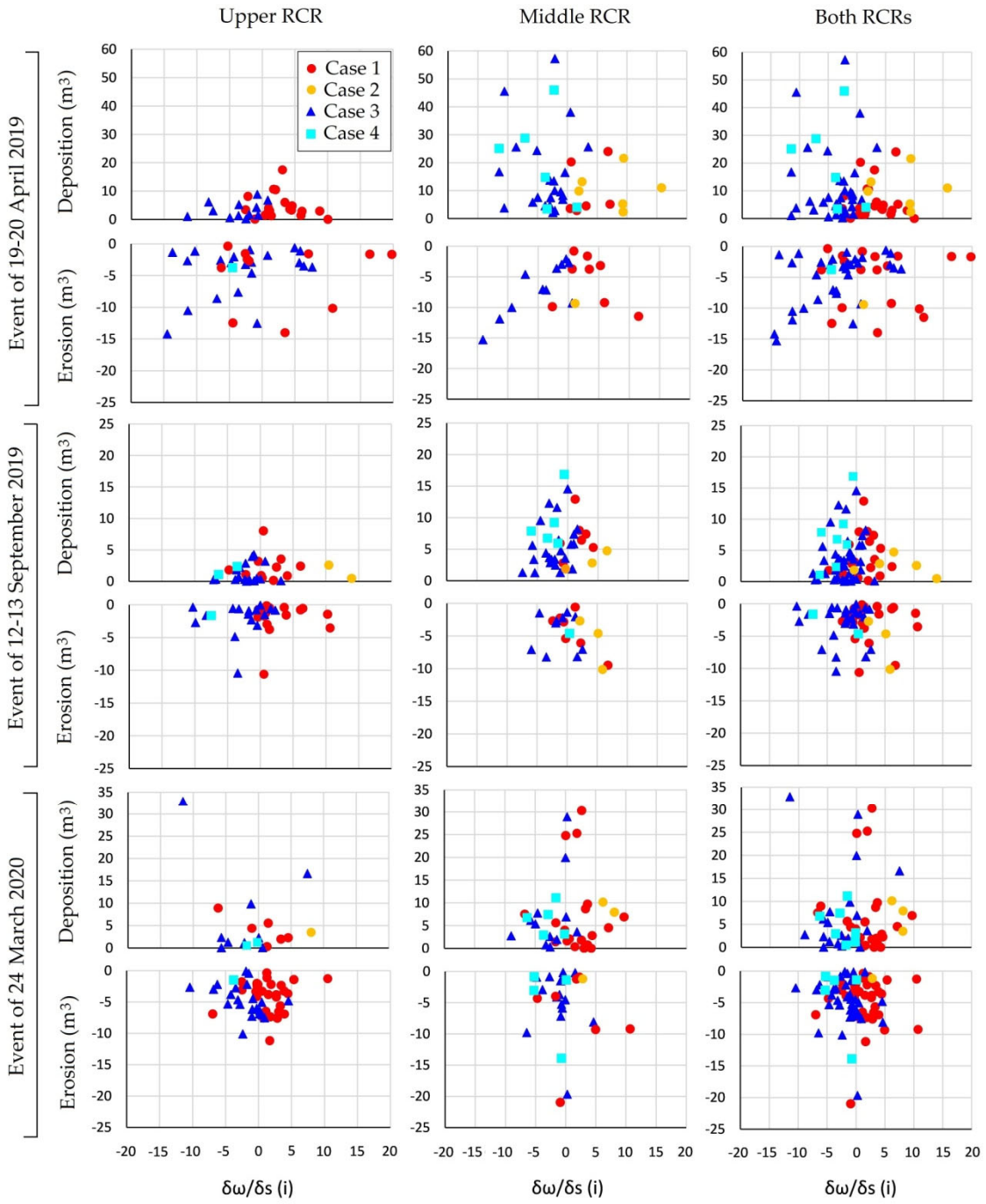

Figure 15. Plots of $\partial\omega/\partial s(i)$ versus E(i+ 1) and D(i + 1) for the three peak flows studied along the upper and middle RCRs and the set of both RCRs. Each symbol represents one of the four conditions listed in Table 2.

Regarding deposition, it was slightly higher in the middle stretch than in the upper section, but the distribution pattern in relation to the energy gradient and the type of case differed considerably between the two channel reaches.

Along the upper RCR the values of D were highest where $\partial\omega/\partial s$ approached zero, and they gradually decreased as the $\partial\omega/\partial s$ values became more positive, which bears some resemblance to the trend described by Lea and Legleiter (2016) for non-ephemeral gravel streams. In contrast, this behavior did not occur in the middle RCR, whose scatter diagram shows a large dispersion of values in all cases. Despite this, the cases representing a minor deposition over a significant accretion dominated here, it being relatively rare thatω decreased downstream and fell below ω_c in cell i (case 4) (Fig. 15). As a result, the middle RCR frequently acted as a sink for material eroded from the closest upstream reach. This is consistent with the results obtained at a large scale by Wilcock and Crowe (2002) and Török et al. (2017), using flume experiments of mixed-size bed sediment, according to which eroded particles tend to be deposited immediately after the erosion zone. There was a lack of a strong and consistent relationship between negative $\partial\omega/\partial s$ values and net deposition in both stretches and all the events. In contrast, the net erosion volumes were always associated with positive values of $\partial\omega/\partial s$ for case 1 at the different flow stages in the reference upper reach but only at the flood discharge in the middle stretch. Energy gradients below 0 produced scour in case 3, when ω exceeded ω_c despite decreasing downstream.

Scatter plots relating lags in ΔV to $\partial\omega/\partial s$ show a limited relationship between these variables at any lag distance between 0 and 3 budget cells (2.5-3.5 m/cell), regardless of the RCR affected. Although the dispersion was high in all cases, we can distinguish two slightly different patterns, according to the RCR. In the upper RCR the net sediment flux, represented in numerous cells by case 3, was more variable as the lag distance increased, passing the 3rd quartile of values from an initial range of +5 to -10 m^3 in cells i to + 10 to -15m^3 in cells i+3.The opposite occurred with the cells depicting case 1, since the starting cells (i) had more dispersed ΔV values in a wide range of $\partial\omega/\partial s$, and the most distant budget cells (i+3) showed a concentration of flux volumes of both signs between -5 and +10 m^3 for $-5 < \partial\omega/\partial s < 10$ W m^{-2}/m.

The spatial variation pattern of ΔV in relation to $\partial\omega/\partial s$ found for the reference MDR was characterized by a lack of change with the immediate lag distance (i+2) (Fig. 16). At most, only a few budget cells i that met the condition in case 4 showed variation in short downstream paths. For cell i+1, all the net flux values, corresponding to this class of cases,

were positive and variable (0 to 45 m^3), most occurring within a relatively narrow negative $\partial\omega/\partial s$ range (between 2 and 7 W m^{-2}/m).

The response immediately downstream (cell i+2) translated into a concentration of ΔV (0 to 20 m^3) for the same range of energy gradient, part of that variability being recovered in the next cell. In addition, isolated lags in high net fluxes belonging to case 3 were marginally significant, the influence of $\partial\omega/\partial s$ declining as the distance increased. These results are not significantly consistent, since the association of ΔV with negative values of $\partial\omega/\partial s$ in cases 1 and 2 and with positive values of $\partial\omega/\partial s$ in cases 3 and 4 suggests that $\partial\omega/\partial s$ was not strongly related to E and D, which agrees with what was shown by Lea and Legleiter (2016).

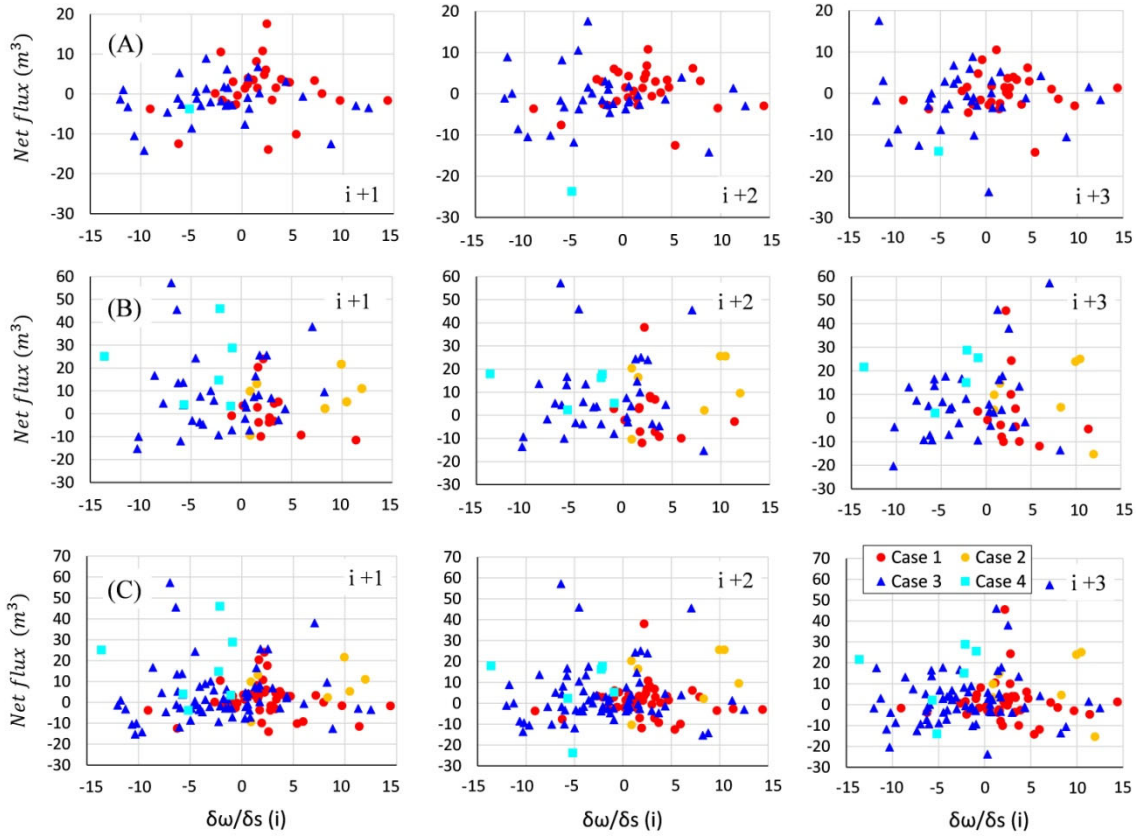

Figure 16. Plots of $\partial\omega/\partial s$(i) (W m^{-2}/m) versus ΔV (i+1 to i+3) (m^3) for the upper (A) and middle (B) reaches and the sum of both channel stretches (C) for the flood of April 2019. These values represent the net sediment fluxes observed for downstream average lags of 3 m (i + 1) to 9 m (i + 3). Each symbol represents one of the four conditions highlighted in Table 2.

Regarding the total net flux, $\partial\omega/\partial s$ (i) maintained the same variation pattern with T as with ΔV (i+1), having a positive sign in the cells encompassed by cases 1 and 2, and a negative

sign in those belonging to cases 3 and 4 (Fig. 17). Normally, we would expect greater values of $\partial\omega/\partial s$ and ε_c to be associated with a larger total flux.

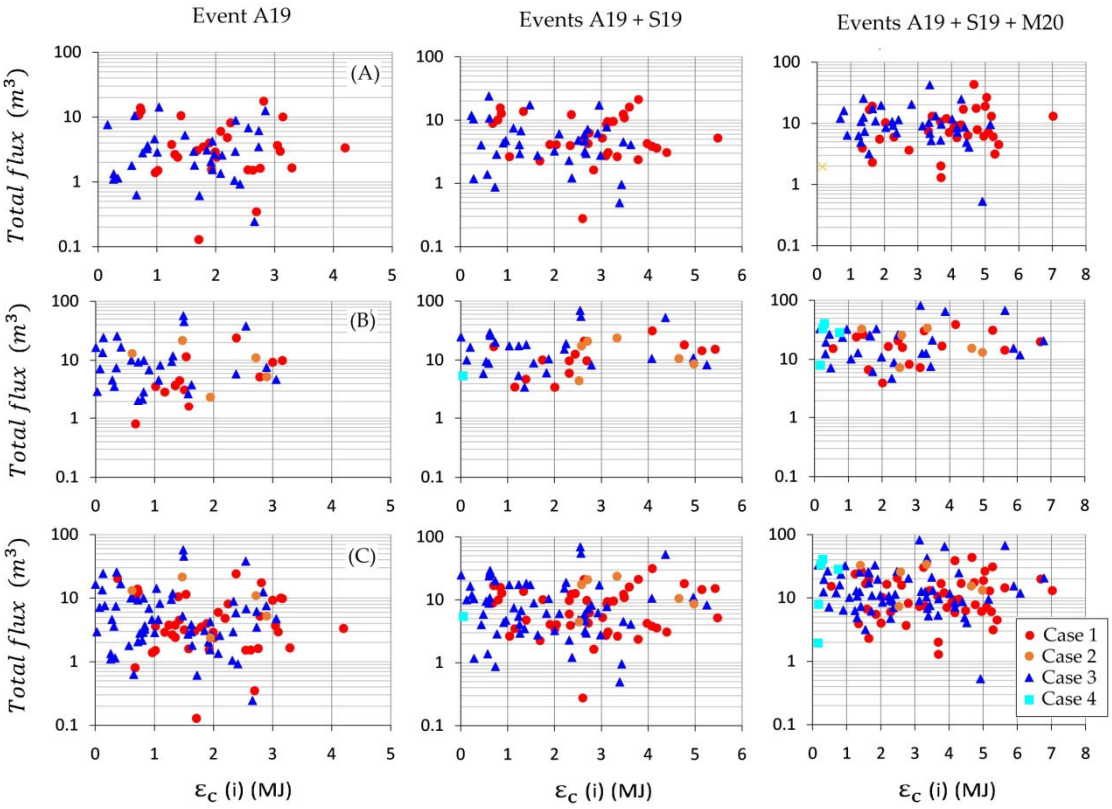

Fig. 17. Plots of T (i + 1) versus ε_c (i) in MJ - for the event of April 2019, the events of April and September, 2019, and all three events analyzed - along the upper (A) and middle (B) reaches and both channel stretches (C). Each symbol represents one of the four conditions listed in Table 3.

However, a high dispersion of these values was a common feature for each channel stretch and study case, as a result of discontinuous changes in bedload and channel morphology. The scattered and skewed distributions of both hydraulic variables could be related to non-homogeneous bed forms or changes in granular texture. Conesa-García et al. (2020b) associated this lack of relationship in another complex gravel-bed dry channel (upper Mula stream, in Southeastern Spain) with the presence of blocks from the bank breaks, pools-riffle sequences, and local transitions from alluvium to substrate outcrop and *vice versa*. Note that the ephemeral stream studied here is characterized by mixed-size bed materials, predominantly gravel, and highly mobile alluvial bars, mostly active bars without vegetation or that are not very stable, that constantly change shape and extension. Especially in the upper reach, isolated groups of blocks deposited by recent collapses or

exhumed ancient boulders disturb the flow regime and alter the total sediment flux over short distances. Zapico et al. (2018) analyzed this type of relationship in a steep, sand-gravel ephemeral channel and found, by contrast, a clear relationship between the variation in bedload flux, texture, and total bedload yield (measured directly in the field) and changes in channel shape and bed texture (derived from topographic surveys using SfM and TLS).

The RBS showed a greater mix of dispersed cases regarding the total sediment yield, perhaps due to a different bed response that released various particle sizes at contrasting critical stresses, versus spatial variations in the mean stream power. As other authors (e.g. Billi, 2011) have verified for ephemeral channels during flash flood events, the bedload here made up most of the total sediment flux. Consequently, variations in the amount and thickness of gravel available for entrainment could lead to fluctuations in the downstream bedload and hence in T values.

In Fig. 16, $\varepsilon_c(i)$ was plotted against T(i) to examine the hypothesis that these two variables could be correlated. All these scatter plots display point clouds, which represent the relationships between these variables for the flood of April 2019, and the two following minor events, for which ε(i) values were added in chronological order. The condition $\omega(i) > \omega(i-1) > \omega_c$ (case 1), which represents an erosional trend, occurs at an ε_c value above 0.2 MJ in the upper RCR and above 0.1 MJ in the middle RCR. Below these thresholds the cumulative excess energy per unit bed area (ε_c) over the flow peak time is insufficient to cause scour, although the movement of the bed material load is negligible. Up to an ε_c value of approximately 1 MJ, budget cells prone to deposition predominated, whereas from this threshold onwards the number of cells with a tendency to suffer erosion increased.

The largest flood, in April 2019, generated a high total net flux, fluctuating between 0.2 and 20 m^3 per cell in the upper reach and between 0.8 and 50 m^3 per cell in the middle section, associated with ε_c values of 0.1 to 3.3 MJ. The event of September 2019 had little impact on the T values. On the other hand, the additional consideration of the bankfull event of March 2020 meant an increase of 1 and 2 MJ in the upper and middle stretches, respectively, and a maximum increase in T of 20 m^3/cell. Along both reaches, in the entire analysis period, a mean T of 12 m^3/cell was mobilized for a mean ε_c of around 3 MJ. The scarcest movement of bed material corresponded to the budget cells belonging to case 4, with the lowest ε_c, and the highest T values to cells 1 and 3, with ε_c values ranging from 3 to 6 MJ. However, the total accumulated flux was quite considerable in relation to the

basin size and the peak flow generated, especially in the middle section, where 1.5 MJ was enough for T(i) to reach 50 m^3. As has been shown in previous studies (Reid and Laronne, 1995), the bed load flux produced in this type of dry stream during torrential flows often exceeds the maximum order of magnitude measured at similar levels of stream power in perennial counterparts.

An ANOVA and the Tukey HSD test were performed to determine if the behavior of each of the four cases of erosion, deposition, and net sediment flux differed among the peak flow events and between the RCRs (Table 8). The results show that there were no significant differences among the means of the four cases for each of the groups identified as variables referring to sediment budgets, which contrasts with the hypothesized conditions from Table 2. By contrast, the cases of the $\partial\omega/\partial s$ group generally reflected a significant relationship, with rejection of the null hypothesis of equality of variances and, therefore, important differences between the cases. Considering the entire period, a closer relationship was found for the cases of deposition in the upper RCR and for the cases of erosion in the middle RCR (Table 9).

Table 8. ANOVA and Tukey range test P-values for the evaluation of whether the means among the four cases described in Table 2 are significantly different for the sediment budget variables in each peak flow and RCR (asterisks represent significant differences, $p < 0.05$).

		19-20 April, 2019				12 September, 2019				24 March, 2020			
		E	D	ΔV	δω/δs	E	D	ΔV	δω/δs	E	D	ΔV	δω/δs
Upper RCR	ANOVA	0.95	0.40	0.14	0.01*	0.93	0.90	0.78	0.01*	0.41	0.74	0.54	0.01*
	1 vs. 2	-	-	-	-	-	0.99	0.81	0.01*	-	1.00	0.75	0.54
	1 vs. 3	0.96	0.40	0.143	0.01*	0.94	0.87	1.00	0.01*	0.76	0.87	0.75	0.15
	1 vs. 4	0.97	-	0.68	0.42	0.99	1.00	0.95	0.01*	0.54	0.97	0.87	0.01*
	2 vs. 3	-	-	-	-	-	0.99	0.80	0.01*	-	0.97	0.88	0.25
	2 vs. 4	-	-	-	-	-	1.00	0.98	0.01*	-	0.99	0.97	0.03*
	3 vs. 4	0.99	-	0.93	0.98	0.98	0.99	0.95	0.32	0.43	0.77	0.99	0.13
Middle RCR	ANOVA	0.73	0.44	0.07	0.01*	0.88	0.83	0.14	0.01*	0.73	0.98	0.63	0.01*
	1 vs. 2	0.71	1.00	0.77	0.26	0.87	0.67	0.79	0.15	0.77	0.99	0.98	0.47
	1 vs. 3	0.94	0.99	0.43	0.01*	1.00	0.99	0.95	0.01*	0.85	1.00	0.68	0.01*
	1 vs. 4	-	0.50	0.04*	0.01*	0.99	0.22	0.26	0.04*	0.92	0.99	0.95	0.08
	2 vs. 3	0.79	0.99	1.00	0.01*	0.88	0.66	0.50	0.01*	0.92	0.99	0.81	0.03*
	2 vs. 4	-	0.54	0.41	0.01*	0.99	0.73	0.10	0.01*	0.94	0.98	0.91	0.04*
	3 vs. 4	-	0.48	0.26	0.99	1.00	0.13	0.37	0.98	1.00	0.99	0.99	0.99

Table 9.ANOVA and Tukey range test P-values for the evaluation of whether the means among the four cases described in Table 2 are significantly different for the sediment budget variables in the entire analysis period and both RCRs (asterisks indicate significant differences, $p < 0.05$).

	29 November 2018 to 26 July 2020							
	Upper RCR				Middle RCR			
	E	D	ΔV	δω/δs	E	D	ΔV	δω/δs
ANOVA	0.62	0.80	0.74	0.01*	0.98	0.30	0.21	0.01*
1 vs. 2	-	0.96	0.78	0.01*	1.00	0.99	0.96	0.01*
1 vs. 3	0.83	0.99	0.98	0.01*	0.99	0.93	0.83	0.01*
1 vs. 4	0.78	0.80	0.99	0.01*	0.98	0.23	0.15	0.01*
2 vs. 3	-	0.98	0.72	0.01*	0.99	0.99	1.00	0.01*
2 vs. 4	-	0.99	0.91	0.01*	0.99	0.59	0.61	0.01*
3 vs. 4	0.66	0.84	0.98	0.33	0.99	0.39	0.34	1.00

Conclusions

It is known that the morphodynamics in ephemeral streams are subject to non-continuous geomorphic activity associated with hydrological events of different magnitudes, discrete in time. Understanding the morphological adjustments derived from such events in ephemeral gravel-bed channels is often complex, due to the influence of variations in the bedload on the location of sediment sources and sinks within the channel, bed armoring, and changes in bedforms. In such cases, the applicability limits of the existing sediment transport formulas still constrain the accuracy of the numerical modeling, making it advisable to adopt a sediment budget approach. In this case study an excess or deficit of sediment at the event scale implied short-term changes in the bed elevation depending on the peak flow. Such changes were satisfactorily evaluated through the combined use of SfM-MVS and TLS, according to the spatial scale and geomorphic scenario. The SfM-MVS technique turned out to be suitable for quantifying sediment budgets in RCRs more than 100 m in length, while TLS provided excellent results for the assessment of changes in bedforms at more detailed spatial scales (e.g. PBSAs). In addition, the VHR DTM generated from the combination of both techniques increased the accuracy of the 1-D hydrodynamic model previously calibrated with field data. The ground-based LiDAR-derived bed elevation change depicted the common trend towards a dynamic equilibrium in the upper RCR and a more variable behavior in the middle section, where sediment transport of more variable bedload composition occurred — both in time and space —. The scatter plots relating $\partial \omega / \partial s$ (i) to Δe(i) and ΔV(i) along the middle RCR showed the sparsest distributions and reflected the smallest lag effect (i+n), which also extended to the morphological response.

Hypotheses concerning the relationships between spatial patterns of stream power and changes in bed elevation and sediment fluxes were tested for different conditions of flow competence. The spatial variation pattern of ΔV with $\partial\omega/\partial s$ was not significantly consistent, since the association of ΔV with negative values of $\partial\omega/\partial s$ in cases 1 and 2 and with positive values of $\partial\omega/\partial s$ in cases 3 and 4 suggests that $\partial\omega/\partial s$ was not strongly related to erosion and deposition rates. However, a different geomorphic response was found in relation to three discharge thresholds. The largest events, with overtopping flows above 30 $m^3\ s^{-1}$, showed the highest values of stream power ($\omega > 300\ Wm^{-2}$) and great spatial variability in both the mean power gradient ($\sigma > 6\ Wm^{-2}/m$) and the excess energy ($\sigma > 80\ Wm^{-2}$). These peak flows mobilized a vast amount of bedload, causing notable transitory erosion and leading to overall vertical accretion. By contrast, ω values from 35 to 150 Wm^{-2}were associated with the removal of bank-failure deposits and moderate changes in active low bars. Bed aggradation especially dominated in the lateral zones, due to bank breakage and displacement of medial gravel bars. Contrarily, moderate peak flows, at the bankfull and sub-bankfull stages, mainly produced surface washing, selective transport, and scour processes. The effective discharge for bed load transport occurred at stages higher than bankfull discharge. If, as is to be expected in southeastern Spain, climate change implies - in the short and medium term - an increase in the frequency of large events to the detriment of low-water discharges, it is most likely that ephemeral gravel-bed streams will undergo processes more typical of arid regions, such as bed degradation, armoring, lateral erosion, and channel widening. In conclusion, this study provides a useful approach to analyze, at the event scale and very spatial resolution, relationships between stream power variations and morphological bed changes in a typically Mediterranean ephemeral gravel-bed stream. Furthermore, the results, also based on changes in bed stability and sediment fluxes, are applicable to protection and restoration plans in a wide range of ephemeral Mediterranean channels, whose recent dynamics reflects the effects of climate change.

Notation

bgu	bed geomorphic unit [-]
D_{50}	median grain size (m)
D_{84}	particle size corresponding to the 84% ofthe sample weight (m)
g	acceleration of gravity [m s^{-2}]
i	cell ati cross-section
j	cell lag at j cross-section
R	hydraulic radius [m]
RBS	relative bed stability index [-]

BFS	bedform stability index [-]
r^2	determination coefficient [-]
S_w	water surface slope [m m^{-1}]
D	gross deposition (m^3)
E	gross erosion (m^3)
Fr	Froude number [-]
PBSA	pilot bed survey area
Q_{pf}	Peak flow discharge (m^3 s^{-1})
RCR	reference channel reach
T	total sediment flux (m^3)
ΔV	net sediment flux (m^3)
$\partial\omega/\partial s$	mean stream power gradient [Wm^{-2}/m]
$\varepsilon_{(i)}$	excess energy per unit bed area over ω_c at cell i [W m^{-2}]
ε_c	cumulative excess energy per unit bed area (MJ)
γ	specific weight of water (N m^{-3}),
Ω	cross-sectional stream power [W m^{-1}]
ω	mean stream power [W m^{-2}]
ω_c	critical mean stream power [W m^{-2}]
ω/ω_c	mean stream power (ω) / resisting power (ω_c) ratio [-]
ρ	density of water [kg m^{-3}]
ρ_s	density of sediment [kg m^{-3}]
υ	flow velocity (m s^{-1})
τ	shear stress (N m^{-2})
τ_{bf}	shear stress at bankfull flow (N m^{-2})
τ_{c84}	critical shear stress required to mobilize D_{84}-size particles (N m^{-2})
τ_c^*	critical values of the dimensionless Shields parameter [-]

Acknowledgments

This work has been financed by ERDF / Spanish Ministry of Science, Innovation and Universities - State Research Agency (AEI) / Project CGL2017-84625-C2-1-R (CCAMICEM); State Program for Research, Development and Innovation focused on the Challenges of Society. We also would like to extend our thanks to AEMET and the Segura River Hydrographic Confederation Center (SHC), Government of Spain, for their collaboration.

References

Billi, P. 2011. Flash flood sediment transport in a steep sand-bed ephemeral stream. International Journal of Sediment Research, 26(2): 193-209. https://doi.org/10.1016/S1001-6279(11)60086-3

Biron, P.M., Choné, G., Buffin-Bélanger, T., Demers, S., Olsen, T., 2013. Improvement of streams hydro-geomorphological assessment using LiDAR DEMs. Earth Surf. Process. Landf. 38, 1808–1821.

Buffington J.M., Montgomery D.R. (1997). A systematic analysis of eight decades of incipient motion studies, with special reference to gravel-bedded rivers. Water Resour Res 33(8): 1993–2029. doi: 10.1029/96WR03190

Camenen, B., Jaballah M., Geay T., Belleudy P., Laronne J.B., and Laskowski J.P. (2012), Tentative measurements of bedload transport in an energetic alpine gravel bed river. In M. Munoz (Ed.), River Flow, pp. 379–386, Taylor & Francis Group, London.

Kasprak, A.; Wheaton, J.M.; Ashmore, P.E.; Hensleigh, J.W.; Peirce, S. 2015. The relationship between particle travel distance and channel morphology: Results from physical models of braided rivers. J. Geophys. Res. Earth Surf., 120, 55–74. https://doi.org/10.1002/2014JF003310

Lea, D.M.; Legleiter, C.J. (2016): Mapping spatial patterns of stream power and channel change along a gravel-bed river in northern Yellowstone. Geomorphology, 252: 66–79. https://doi.org/10.1016/j.geomorph.2015.05.033

Leopold, L.B.; Wolman, M.G.; Miller, J.P. (1964): Fluvial Processes in Geomorphology; Dover Publications: New York, NY, USA. 544 p.

Proyecto NATMUR (2008): Catálogo de Geoservicios de Medio Natural, Vuelofotogramétrico Digital y levantamiento LIDAR de la Región de Murcia. Available online: http://www.murcianatural.carm.es/natmur08/ (accessed on 20 May 2019).

SCS (Soil Conservation Service). National Engineering Handbook; Section 4.; U.S. Department of Agriculture: Washington, DC, USA, 1972. Available online: https://directives.sc.egov.usda.gov/OpenNonWebContent.aspx?content=18393.wba (accessed on 12 December 2019).

Segura-Beltrán, F.; Sanchis-Ibor, C. Assessment of channel changes in a Mediterranean ephemeral stream since the early twentieth century. The Rambla de Cervera, eastern Spain. Geomorphology **2013**, 201, 199–214. https://doi.org/10.1016/j.geomorph.2013.06.021.

USACE (US Army Corps of Engineers). HEC-RAS, Rivers Analysis System. Hydraulic Reference Manual, Version 5.0; Hydrologic Engineering Center: Davis, CA, USA, 2016.

Benito, G., Thorndycraft, V. R., Rico, M. T., Sanchez-Moya, Y., ´ Sopena, A., Botero, B. A., Machado, M. J., Davis, M., and Pérez-González, A. (2011): Hydrological response of a dryland ephemeral river to southern African climatic variability during the last millennium, Quaternary Research, 75(3): 471-483, doi:10.1016/j.yqres.2011.01.004.

Conesa-Garcia, C. (1995): Torrential flow frequency and morphological adjustments of ephemeral channels in southeast Spain. In River Geomorphology; Hickin, E.J., Ed.; John Wiley & Sons: Chichester, UK, pp. 169–192.

Parker, C.; Clifford, N.J.; Thorne, C.R. (2011): Understanding the influence of slope on the threshold of coarse grain motion: Revisiting critical stream power. Geomorphology, 126, 51–65. https://doi.org/10.1016/j.geomorph.2010.10.027

Schumm, S.A. 1961. Effect of sediment characteristics on erosion and deposition in ephemeral stream channels. United States Geological Survey, Professional Paper, 352C, 31-70. https://doi.org/10.3133/pp352C

Rickenmann, D. (2011), Alluvial steep channels: Flow resistance, bedload transport prediction and transition to debris flows, in Gravel Bed Rivers: Processes, Tools, Environment, edited by M. Church, P. Biron, and A. Roy, John Wiley & Sons, Chichester, England.

Wohl, E. Mountain Rivers; American Geophysical Union: Washington, DC, USA, 2000.

Finnegan, N. J., Roe, G., Montgomery, D.R.and Hallet, B. (2005): Controls on the channel width of rivers: Implications for modeling fluvial incision of bedrock, Geology, 33, 229–232.

Notebaert, B., Verstraeten, G., Govers, G., Poesen, J. (2009): Qualitative and quantitative applications of LiDAR imagery in fluvial geomorphology. Earth Surface Processes and Landforms, 34, 217-231, doi: 10.1002/esp.1705.

Conesa-García, C., Pérez-Cutillas, P., García-Lorenzo, R., Eekhout, J., Gómez-Gutiérrez, A., Millares-Valenzuela, A. and Martínez-Salvador, A. (2020b): Dimensionless morphological ratios versus stream power variations at bankfull stage in an ephemeral channel. *Geomorphology 361*, https://doi.org/10.1016/j.geomorph.2020.107199.

Olsen, D.S., Whitaker, A.C. and Potts, D.F. 1997. Assessing Stream Channel Stability Thresholds Using Flow Competence Estimates at Bankfull Stage. Journal of the American Water Resources Association, 33: 1197-1207. https://doi.org/10.1111/j.1752-1688.1997.tb03546.x

Singer, M.B.; Michaelides, K. 2014. How is topographic simplicity maintained in ephemeral dryland channels?. Geology, 42(12): 1091–1094. https://doi.org/10.1130/G36267.1

Török, G.T., Baranya, S. and Rüther, N. (2017): 3D CFD Modeling of Local Scouring, Bed Armoring and Sediment Deposition. *Water*, *9*(1), 56. https://doi.org/10.3390/w9010056

Wilcock, P.R.; Crowe, J.C. (2003): Surface-based transport model for mixed-size sediment. J. Hydraul. Eng., 129, 120–128.

SCS (Soil Conservation Service) (1972): National Engineering Handbook, Section 4. U.S. Department of Agriculture, Washington, D.C.

Martín-Vide, J.P. (2007): Ingeniería Fluvial. Aspectos técnicos y medioambientales. International Centre for Numerical Methods in Engineering (CIMNE), Universitat Politècnica de Catalunya, Barcelona.

Lague, D. (2014): The stream power river incision model: evidence, theory and beyond, Earth Surface Processes and Landforms, 39: 38-61. DOI: 10.1002/esp.3462.

Almedeij, J.H. (2002): Bedload transport in gravel-bed streams under a wide range of Shields stresses. Doctoral Thesis, Virginia Polytechnic Institute and State University, Virginia. 113 p.

Bizzi, S., Lerner, D.N., 2015. The use of stream power as an indicator of channel sensitivity to erosion and deposition processes. River Research and Applications, 31 (1): 16 – 27. http://dx.doi.org/10.1002/rra. 2717.

Emmett, W.W. and Wolman, M.G. (2001): Effective discharge and gravel-bed rivers. Earth Surface Processes and Landforms, 26(13): 1369-1380, https://doi.org/10.1002/esp.303

Norman, L.M., Sankey, J.B. Dean, D., Caster, J., De Long, S., De Long, W., Pelletier, J.D. (2017): Quantifying geomorphic change at ephemeral stream restoration sites using a coupled-model approach. Geomorphology, 283: 1-16. https://doi.org/10.1016/j.geomorph.2017.01.017

Seifert, E.; Seifert, S.; Vogt, H.; Drew, D.; Van Aardt, J.; Kunneke, A.; Seifer, T. (2019). Influence of drone altitude, image overlap, and optical sensor resolution on multi-view reconstruction of forest images. Remote Sensing, 11(10):1252, doi:10.3390/rs11101252.

Lotsari, E.S., Calle, M., Benito, G., Kukko, A., Kaartinen, H., Hyyppä, J., Hyyppä, H., and Alho, P. (2018): Topographical change caused by moderate and small floods in a gravel bed ephemeral river – a depth-averaged morphodynamic simulation approach. Earth Surf. Dynam., 6, 163–185, https://doi.org/10.5194/esurf-6-163-2018.

Ali, K.F.; De Boer, D.H. Construction of sediment budgets in large-scale drainage basins: The case of the upper Indus River. In Proceedings of the Erosion Prediction in Ungauged Basins: Integrating Methods and Techniques, Montpellier, France, 8–9 July 2003.

Sutfin, N.A., Shaw, J., Wohl, E.E., Cooper, D. (2014): A geomorphic classification of ephemeral channels in a mountainous, arid region, southwestern Arizona, USA. Geomorphology, 221: 164-75. https://doi.org/10.1016/j.geomorph.2014.06.005

Conesa-García, C., Puig-Mengual, C., Riquelme, A., Tomás, T., Martínez-Capel, F., García-Lorenzo, R., Pastor, J.L., Pérez-Cutillas, P. and Cano-Gonzalez, M. (2020): Combining SfM photogrammetry and terrestrial laser scanning to assess event-scale sediment budgets along a gravel-bed ephemeral stream. Remote Sensing 12(21): 3624. https://doi.org/10.3390/rs12213624.

Galea, A.B., Sadler, J.P., Hannah, D.M., Datry, T., Dugdale, S.J. (2019): Mediterranean intermittent rivers and ephemeral streams: Challenges in monitoring complexity. Ecohydrology, 12(8): e2149. https://doi.org/10.1002/eco.2149

Garzón, G.; Alonso, A. Comparison of the flood response of a braided and a meandering river, conditioned by anthropogenic and climatic changes. In Martini, I.P., Baker, V.R., Garzón, G., Eds., Flood and Megaflood Processes and Deposits: Recent and Ancient Examples. Blackwell Publishing Ltd.: Oxford, UK, 2002; p. 320.

Gomez, B., Coleman, S.E., Sy, V.W.K. and Kent, M. (2007): Channel change, bankfull and effective discharges on a vertically accreting, meandering, gravel-bed river. Earth Surface Processes and Landforms 32(5): 770-785. https://doi.org/10.1002/esp.1424

Flatley, A. and Rutherfurd, I. (2018): Using Structure from Motion (SfM) to capture high resolution geomorphic units within small ephemeral channels. 20th EGU General Assembly, EGU2018, Proceedings from the conference held 4-13 April, 2018 in Vienna, Austria, p.10896.

Levick, L.R., Goodrich, D.C., Mariano Hernandez, M., Pima, J.F., Semmens, D.J., Stromberg, J., Tluczek, M., Leidy, R.A., Scianni, M., Guertin, D.Ph., Kepner, W.G., 2008. The Ecological and Hydrological Significance of Ephemeral and Intermittent Streams in the Arid and Semi-Arid American Southwest. U.S. Environmental Protection Agency, Office of Research and Development, Washington, p. 101.

Lisle, T.E.; Church, M. 2002. Sediment transport-storage relations for degrading, gravel bed channels. Water Resources Research, 38(11): 1219, doi: 10.1029/2001WR001086.

Calle, M., Alho, P., Benito, G. (2018): Monitoring ephemeral river changes during floods with SfM photogrammetry. Journal of Iberian Geology, 44(3), 355-373. https://doi.org/10.1007/s41513-018-0078-y

Golly, A.; Turowski, J.M. 2017. Deriving principle channel metrics from bank and long-profile geometry with the R-package cmgo. Earth Surf. Dynam. 5, 557–570.

Salmela, J., Kasvi, E., Vaaja, M. T., Kaartinen, H., Kukko, A., Jaakkola, A., Alho, P. (2020): Morphological changes and riffle-pool dynamics related to flow in a meandering river channel based on a 5-year monitoring period using close-range remote sensing. Geomorphology, 352, 106982. https://doi.org/10.1016/j.geomorph.2019.106982

Ortega, J.A., Razola, L., Garzón, G., 2014. Recent human impacts and change in dynamics and morphology of ephemeral rivers. Nat. Hazards Earth Syst. Sci. 14 (3), 713–730.

Rowley, T., Ursic, M., Konsoer, K., Langendon, E., Mutschler, M., Sampey, J., Pocwiardowski, P. (2020): Comparison of terrestrial lidar, SfM, and MBES resolution and accuracy for geomorphic analyses in physical systems that experience subaerial and subaqueous conditions. Geomorphology, 355, 107056, https://doi.org/10.1016/j.geomorph.2020.107056

Rusnák, M., Sládek, J., Kidová, A., Lehotský, M. (2018): Template for High-Resolution River Landscape Mapping Using UAV Technology. Measurement: Journal of the International Measurement Confederation 115: 139–151. DOI:10.1016/j.measurement.2017.10.023.

Vázquez-Tarrío, D., Borgniet, L., Liébault, F., Recking, A. (2017): Using UAS optical imagery and SfM photogrammetry to characterize the surface grain size of gravel bars in a braided river (Vénéon River, French Alps). Geomorphology, 285: 94-105. doi:10.1016/j.geomorph.2017.01.039.

Clapuyt, F., Vanacker, V., Van Oost, K. (2016): Reproducibility of UAV-based earth topography reconstructions based on Structure-from-Motion algorithms. Geomorphology, 260: 4-15. doi: https://doi.org/10.1016/j.geomorph.2015.05.011.

Egeler, C.G. and Simon, O.J. (1969): Orogenic evolution of the Betic Zone (Betic Cordilleras, Spain), with emphasis on the nappe structures. Geologie en Mijnbouw, 48: 296-305.

Reid, I., and Laronne, J.B. (1995). Bedload sediment transport in an ephemeral stream and a comparison with seasonal and perennial counterparts. Water Resources Research 31, 773-81. https://doi.org/10.1029/94WR02233

Zapico I., Laronne J.B., Lucía A., Martín-Duque J.F. (2018). Morpho-textural implications to bedload flux and texture in the sand-gravel ephemeral Poveda Gully. Geomorphology, 322: 53-65. doi:10.1016/j.geomorph.2018.08.026

Hooke, J.M. 2006. Human impacts on fluvial systems in the Mediterranean region. Geomorphology, 79: 311–335.

Pitlick, J. and Cress, R. 2002. Downstream changes in the channel geometry of a large gravel bed river. Water Resources Research, 38(10): 34-1-34-11, https://doi.org/10.1029/2001WR000898

Puig-Mengual, C.A., Woodget, A.S., Muñoz-Mas, R. and Martínez-Capel, F. (2021): Spatial validation of submerged fluvial topographic models by mesohabitat units. International Journal of Remote Sensing, 42(7): 2391-2416, DOI: 10.1080/01431161.2020.1862433

Vázquez-Tarrío, D., Borgniet, L., Liébault, F. and Recking, A. 2017. Using UAS Optical Imagery and SfM Photogrammetry to Characterize the Surface Grain Size of Gravel Bars in a Braided River (Vénéon River, French Alps). Geomorphology 285: 94–105. doi:10.1016/j.geomorph.2017.01.039.

Wheaton, J.M., Brasington, J., Darby, S.E., Sear, D.A., 2010b. Accounting for uncertainty in DEMs from repeat topographic surveys: improved sediment budgets. Earth Surface Processes and Landforms 35 (2), 136–156.

Woodget, A.S., and Austrums, R. (2017): Subaerial Gravel Size Measurement Using Topographic Data Derived from a UAV-SfM Approach. Earth Surface Processes and Landforms 42 (9): 1434–1443. doi:10.1002/esp.4139.

Woodget, A.S., Dietrich, J.T. and Wilson, R.T. (2019): Quantifying below-water fluvial geomorphic change: the implications of refraction correction, water surface elevations, and spatially variable error. Remote Sensing, 11(20): 2415, https://doi.org/10.3390/rs11202415

Magilligan, F.J. 1992: Thresholds and the spatial variability of flood power during extreme floods, Geomorphology, 5, 373–390.

Stacey, M. and Rutherfurd, I. 2007: Testing specific stream power thresholds of channel stability with GIS, 5th Annual Australian Stream Management Conference, Albury, Australia, 384–389.

Rojan, E., Dłużewski, M., Krzemień, K. (2020): Sediment budget of high mountain stream channels in an arid zone (High Atlas mountains, Morocco. Catena. 190, July 2020, 104530. https://doi.org/10.1016/j.catena.2020.104530.

Tooth, S. (2000), Downstream changes in dryland river channels: The Northern Plains of arid central Australia, Geomorphology, 34(1-2): 33 - 54. https://doi.org/10.1016/S0169-555X(99)00130-0

Lotsari, E., Thorndycraft, V., and Alho, P. (2015): Prospects and challenges of simulating river channel response to future climate change, Progress in Physical Geography, 39: 483–513, https://doi.org/10.1177/0309133315578944.

Brodu, N.; Lague, D. 3D terrestrial lidar data classification of complex natural scenes using a multi-scale dimensionality criterion: Applications in geomorphology. ISPRS J. Photogramm. Remote Sens. **2012**, 68, 121–134.

Lague, D., Brodu, N. and Leroux, J.J. 2013: Accurate 3D comparison of complex topography with terrestrial laser scanner: Application to the Rangitikei canyon (NZ) ISPRS Journal of Photogrammetry and Remote Sensing, 82 1026, doi:10.1016/j.isprsjprs.2013.04.009

Girardeau-Montaut D. 2020. CloudCompare – 3D Point Cloud and Mesh Processing Software (Version 2.11.3). GPL Software. 2020. Open Source Project, http://www.cloudcompare.org/ [14.10.2020]

Conesa-García, C. and García-Lorenzo, R. (2009). Effectiveness of check dams in the control of general transitory bed scouring in semiarid catchment areas (South-East Spain). Water and Environment Journal, 23(1): 1-14.

Pryor, B.S., Lisle, T., Montoya, D.S., and Hilton, S. (2014): Transport and storage of bed material in a gravel bed channel during episodes of aggradation and degradation: a field and flume study. Earth Surface Processes and Landforms, 36: 2028–2041. doi: 10.1002/esp.2224.